Idealized Aquaplanet Simulations of Tropical Cyclone Activity: Significance of Temperature Gradients, Hadley Circulation, and Zonal Asymmetry

GAN ZHANG,[a,b,c] LEVI G. SILVERS,[a,d] MING ZHAO,[b] AND THOMAS R. KNUTSON[b]

[a] *Atmospheric and Oceanic Sciences Program, Princeton University, Princeton, New Jersey*
[b] *National Oceanic and Atmospheric Administration/Geophysical Fluid Dynamics Laboratory, Princeton, New Jersey*

(Manuscript received 11 March 2020, in final form 15 December 2020)

ABSTRACT: Earlier studies have proposed many semiempirical relations between climate and tropical cyclone (TC) activity. To explore these relations, this study conducts idealized aquaplanet experiments using both symmetric and asymmetric sea surface temperature (SST) forcings. With zonally symmetric SST forcings that have a maximum at 10°N, reducing meridional SST gradients around an Earth-like reference state leads to a weakening and southward displacement of the intertropical convergence zone. With nearly flat meridional gradients, warm-hemisphere TC numbers increase by nearly 100 times due particularly to elevated high-latitude TC activity. Reduced meridional SST gradients contribute to a poleward expansion of the tropics, which is associated with a poleward migration of the latitudes where TCs form or reach their lifetime maximum intensity. However, these changes cannot be simply attributed to the poleward expansion of Hadley circulation. Introducing zonally asymmetric SST forcings tends to decrease the global TC number. Regional SST warming—prescribed with or without SST cooling at other longitudes—affects local TC activity but does not necessarily increase TC genesis. While regional warming generally suppresses TC activity in remote regions with relatively cold SSTs, one experiment shows a surprisingly large increase of TC genesis. This increase of TC genesis over relatively cold SSTs is related to local tropospheric cooling that reduces static stability near 15°N and vertical wind shear around 25°N. Modeling results are discussed with scaling analyses and have implications for the application of the ''convective quasi-equilibrium and weak temperature gradient'' framework.

KEYWORDS: Cyclogenesis/cyclolysis; Hadley circulation; Tropical cyclones; Vortices; General circulation models; Climate variability

1. Introduction

Idealized simulations can provide attractive opportunities to evaluate global climate models and understand complex atmospheric dynamics (Held and Suarez 1994; Neale and Hoskins 2000; Blackburn and Hoskins 2013). Using horizontal grid spacing around 50 km, recent aquaplanet models can explicitly simulate tropical cyclones (TCs) or TC-like vortices, leading to interesting insights into climate controls of TC activity (Merlis and Held 2019). These existing TC-permitting aquaplanet simulations mostly used prescribed ocean forcings, which are often spatially homogeneous (e.g., Shi and Bretherton 2014; Merlis et al. 2016; Chavas and Reed 2019) or zonally symmetric (e.g., Merlis et al. 2013; Ballinger et al. 2015; Fedorov et al. 2019). Despite the popularity of these idealized forcings, it is noteworthy that Earth's ocean surface has meridional and zonal heterogeneity that varies from year to year and throughout the geological history. To move toward connecting TC activity in aquaplanet simulations and TC activity in the real-world Earth, it is important to explore both zonally symmetric and asymmetric forcings.

The existing aquaplanet TC studies often prescribe oceanic forcings in the form of idealized SSTs or oceanic heat flux in slab-ocean models. These settings can be tuned to simulate climates that have some ''Earth-like'' features, such as an intertropical convergence zone (ITCZ), or the tropical ascent branch of the Hadley circulation. Merlis et al. (2013) and Ballinger et al. (2015) showed that a northward displacement (and intensification) of the ITCZ increases the TC genesis number in their aquaplanet simulations. Although this ITCZ–TC relationship is mostly consistent with the observational findings in the North Atlantic and the Northeastern Pacific basins (Zhang and Wang 2013, 2015), Fedorov et al. (2019) showed that the relationship does not hold when different sea surface temperature (SST) profiles were prescribed to a different aquaplanet model. In particular, Fedorov et al. (2019) found that a decrease of meridional SST gradients weakens the ITCZ and shifts it equatorward from the summer hemisphere, but the ITCZ changes are accompanied by an overall *increase* of TC genesis related to a poleward migration of TC genesis. The increase of TC genesis at high latitudes appears related to changes in SST, midtroposphere humidity, and vertical wind shear. It is, however, unclear whether the findings documented by Fedorov et al. (2019) depend on their unique model settings (i.e., hypohydrostatic rescaling and no convective parameterization) or depend on their SST profiles, which differ from preceding studies.

A careful comparison of the climate–TC relationship in aquaplanet simulations and the real world may help to improve our physical understanding. Besides the aforementioned

[c] Current affiliation: Citadel Americas, LLC, Chicago, Illinois.
[d] Current affiliation: School of Marine and Atmospheric Sciences, Stony Brook University, State University of New York, Stony Brook, New York.

Corresponding author: Gan Zhang, ganzhang@princeton.edu

DOI: 10.1175/JAS-D-20-0079.1

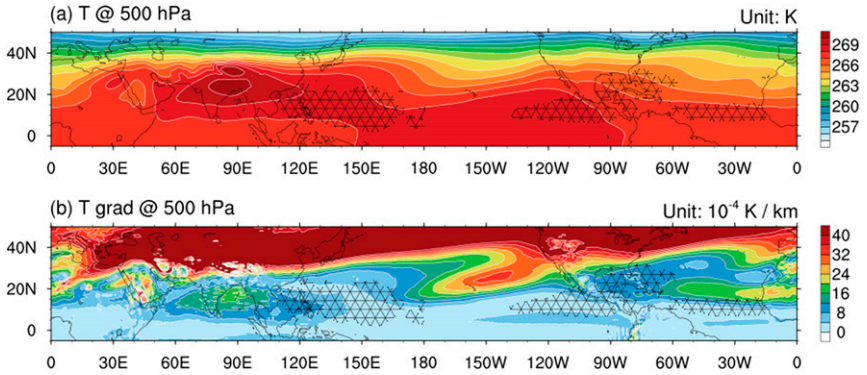

FIG. 1. July–October climatology of (a) 500-hPa air temperature (K; shading) and (b) the magnitude of its horizontal gradients (10^{-4} K km^{-1}; shading). The 500-hPa temperature data are from the ERA-Interim (Dee et al. 2011) and used to approximate the mean temperature of the free troposphere. Hatching highlights the 5° × 5° gridded regions where TCs form at least once per 20 years. All the calculations use July–October data from 1979 to 2013.

ITCZ–TC relationship, a meaningful comparison could examine the relationship between the meridional extent of the Hadley circulation and the latitude where TCs attain their lifetime maximum intensity (LMI). Based on observational data, Kossin et al. (2014) reported a poleward migration of the LMI latitudes and suggested the change might be associated with a poleward expansion of the tropics. Nonetheless, the interpretation of the observational findings is complicated by the unforced natural variability and the basin-to-basin variability (Moon et al. 2015; Studholme and Gulev 2018). Interestingly, the poleward migration of the LMI location also appears related to a poleward migration of TC genesis (Daloz and Camargo 2018; Studholme and Gulev 2018). These changes were tied to the expansion of the Hadley circulation (Studholme and Gulev 2018; Sharmila and Walsh 2018), which was robustly projected by climate models under global warming (e.g., Lu et al. 2007; Hu et al. 2013). A thorough evaluation of these climate–TC relations with full-fledged climate models is much needed, but this approach remains difficult because of high computing costs and significant model biases that involve complex dynamics. As an exploratory intermediate step, it would be useful to investigate if these previously identified climate–TC relations are present in aquaplanet simulations with simple zonally symmetric forcings.

With or without zonally symmetric forcings, the tropical upper troposphere of Earth tends to maintain a nearly zonally symmetric state. As the low-latitude values of the Coriolis parameter are small, the horizontal heterogeneity of the tropical atmosphere is limited under the geostrophic balance (Charney 1963; Held and Hoskins 1985; Sobel and Bretherton 2000). Generally speaking, deviations from the weak temperature gradient (WTG) state (e.g., convective perturbations) tend to be rapidly homogenized by internal gravity waves (Schubert et al. 1980; Bretherton and Smolarkiewicz 1989; Mapes 1993). Even though there are some exceptions related to rotating disturbances (Raymond et al. 2015), the WTG state reasonably approximates the tropical upper atmosphere and affords an elegant simplification of the large-scale tropical dynamics (e.g., Bretherton and Sobel 2002; S. Wang et al. 2013; Herman and Raymond 2014). When combined with the convective quasi-equilibrium (CQE) concept (Arakawa and Schubert 1974; Emanuel et al. 1994)—which ties the tropospheric temperature to the boundary layer moist static energy—the WTG constraint of the upper troposphere dictates that tropical precipitating regions share similar values of subcloud moist static energy (Byrne and O'Gorman 2013; Emanuel 2019; Zhang and Fueglistaler 2020).

Since TCs are an extreme form of tropical convection and develop from weaker convective systems, it is conceivable that the CQE-WTG framework can help to explain changes in TC activity. More specifically, tropical SST variations (e.g., El Niño–Southern Oscillation) affect convective activity and the temperature profile of the overlying atmosphere via the CQE. The associated upper-tropospheric temperature anomalies are thought to spread across the tropics nearly homogeneously under the WTG constraint. These resulting tropics-wide responses of upper-troposphere temperature can modulate the static stability in remote tropical regions—and ultimately affect convective activity (e.g., Johnson and Xie 2010; Wang and Sobel 2011; Fueglistaler et al. 2015) and TC activity (e.g., Tang and Neelin 2004). As this tropical teleconnection mechanism involves the relative difference between local and remote SSTs, it is also referred to as the relative SST mechanism (Vecchi et al. 2008). Notably, this mechanism can modulate convective systems that precede TCs. This reasoning differs from treating the relative SST as a proxy of the maximum potential intensity (MPI) (Emanuel 1988; Vecchi and Soden 2007), which is sensitive to changes of relative SST under the WTG assumption (Ramsay and Sobel 2011).

Although the WTG state is sometimes reduced to a zero-gradient state for simplicity, regional temperature variations certainly exist with zonally asymmetric boundary conditions, especially at off-equator latitudes. Figure 1a shows the climatological tropospheric temperature during July–October from the ERA-Interim (Dee et al. 2011). While the WTG approximation holds well for most tropical regions, the temperature field poleward 10°N has a distinctive zonally varying structure that involves relatively warm and cold regions. These regions

correspond to stationary monsoon ridge and midocean trough structures that are part of the planetary-scale Rossby waves (e.g., Rodwell and Hoskins 2001). These zonally asymmetric features are subject to the influences of both tropical SSTs (e.g., B. Wang et al. 2013) and the extratropical atmosphere (e.g., Schneider and Bordoni 2008). At the periphery of these ridges and troughs, relatively large temperature gradients exist in regions including the tropical central Pacific (180°) and the South Asian monsoon region (90°E) (Fig. 1b). Interestingly, the regions with relatively large temperature gradients are characterized by suppressed TC activity. The temperature gradients at the TC-prone latitudes (10°–25°N) are mostly related to meridional temperature differences (Fig. 1a), which did not receive much attention in the past WTG literature. Meanwhile, changes in the off-equator temperature gradients in model projections of future climate can be large but highly uncertain (Ma and Xie 2013). It is conceivable to use idealized model settings to explore how well the tropical free-tropospheric temperature conforms with the CQE-WTG picture and whether any deviations in off-equator regions might have interesting implications for TC activity.

Zonally varying climates can be approximated using aquaplanet simulations forced by zonally asymmetric SST forcings (Neale and Hoskins 2000). This simplification has proven useful for studying the weather/climate variations associated with the Northern Hemisphere summertime monsoon circulation and its responses to external forcings (e.g., Shaw and Voigt 2015; Wu and Shaw 2016; Chen et al. 2017). Here we will investigate whether the model setting can help to elucidate the sensitivity of TC activity to zonally asymmetric forcings. Such an investigation may pave the way for using the aquaplanet setting to study how oceanic equatorial modes (e.g., El Niño–Southern Oscillation) and meridional modes (e.g., Pacific and Atlantic meridional modes; Chiang and Vimont 2004) can affect local and remote TC activity (e.g., Gray 1984; Vimont and Kossin 2007). Furthermore, this investigation might shed light on some puzzling behaviors of TC activity in or near monsoon regions, such as the *negative* correlation between TC activity and local SST in the Northwestern Pacific (Sharmila and Walsh 2017).

As a step toward connecting aquaplanet simulations and the aforementioned real-world questions, this study carries out aquaplanet general circulation model (GCM) experiments with both zonally symmetric and zonally asymmetric SST forcings. These experiments are conducted with a high-resolution (50-km grid spacing) version of an atmospheric model that was recently developed at Geophysical Fluid Dynamics Laboratory (GFDL; Zhao et al. 2018b; Zhao 2020). These experiments serve as an assessment of our climate model and physical understanding. Our investigation is broadly guided by the following two questions.

1) Do *zonally symmetric* SST forcings produce the relationship between TC activity and the Hadley circulation (or the ITCZ) outlined by the previous aquaplanet and observational studies?
2) Do *zonally asymmetric* SST forcings replicate the relative SST mechanism that has been used for interpreting relationships between changes in SST and TC activity?

Our model simulations are complemented with simple scaling analyses that highlight the nature of the summer atmospheric circulation and the significance of tropical temperature gradients. The discussion will emphasize climate dynamics and some features that contradict the conventional understanding of the TC–climate relationship. The rest of the paper is organized as follows. Section 2 describes the model settings, SST forcing, and the TC tracking algorithm. Sections 3 and 4 present the experiment results with our zonally symmetric and zonally asymmetric forcings, respectively. Section 5 offers a summary and discussion.

2. Data and methodology

a. Model settings

This study leverages AM4, a recently developed global atmospheric model from GFDL. The model has a cubed-sphere atmospheric dynamical core with 33 vertical levels. When forced by observed SSTs and other boundary conditions, the standard 100-km-grid version of AM4 can simulate the climatology, seasonal cycle, and interannual variability of TC activity fairly realistically (Zhao et al. 2018a). A 50-km-resolution version of AM4 was used for GFDL's participation in CMIP6 HighResMIP and has been documented in Zhao (2020). The model settings used in our aquaplanet simulations (AM4.0-Aqua) are nearly identical to Zhao (2020) except for the following modifications: (i) we exclude the aerosol forcing and hold the carbon dioxide at the level of 348 ppm, which approximately corresponds to the 1990 level; and (ii) our simulations use a realistic diurnal cycle that repeats the radiative forcing of 1 August 1990, which is near the peak of TC activity in the present-day Northern Hemisphere. At the cost of not simulating the seasonal cycle, these simple settings help the model reach equilibria quickly. As will be illustrated in sections 3 and 4, our simulations reach climate equilibria within 2–3 months. This allows sampling a variety of SST forcings and a large population of TCs at relatively low computing expenses.

b. Prescribed SST

For both zonally symmetric and zonally asymmetric forcings, we prescribe SSTs to the AM4.0-Aqua directly using analytical functions. Table 1 presents a list of these idealized SST forcings and their possible connections with the real-world and simulated climates (or climate phenomena). More details of these idealized SST forcings are as follows.

In our experiments with zonally symmetric SSTs, we use a function in the following form:

$$T(\phi) = \begin{cases} a\left\{1 - \sin^2\left[\dfrac{\pi b(\phi - \phi_0)}{180}\right]\right\} + 273.16, & \phi_0 - \dfrac{90}{b} \le \phi \le \phi_0 + \dfrac{90}{b} \\ 273.16, & \text{else} \end{cases}, \tag{1}$$

TABLE 1. List of SST forcings used in aquaplanet experiments.

Zonally symmetric		Zonally asymmetric	
$b = 0.3$[a]	$b = 1.2$[d]	$b = 0.85$, $X = 2$ K	
$b = 0.5$	$b = 1.5$	W1C1–0N[f]	W1C0–0N[h]
$b = 0.7$	$b = 2.0$	W1C1–10N	W1C0–10N[h]
$b = 0.85$[b]	$b = 3.0$	W1C1–20N[g]	W1C0–20N[h]
$b = 1.0$[c]	$b = 4.0$[e]	W1C1–30N[g]	W1C0–30N[h]

[a] Nearly homogeneous SST. RCE-like "TC" world.
[b] Earth-like, but with a warmer extratropics. Possibly similar to future climate with amplified polar warming.
[c] Earth-like, but with milder midlatitude gradients relative to the present climate.
[d] Earth-like, but with a colder extratropics. Possibly similar to the Last Glacial Maximum.
[e] Sharp subtropical SST gradients. Moist baroclinic wave world.
[f] Similar to El Niño–Southern Oscillation.
[g] Similar to the Asia–Pacific monsoon.
[h] Similar to regional warming of tropical oceans.

where T (K) is the SST as a function of latitude ϕ (−90° to +90°), i.e. 90°S to 90°N, a (K) determines the magnitude of SST deviations from the baseline (273.16 K), b sets the meridional gradient of SST, and ϕ_0 (°) is the latitude where the SST maximum resides. The meridional profile (by design) differs from those profiles used by Neale and Hoskins (2000), Ballinger et al. (2015), and Fedorov et al. (2019), as we intend to explore a broader parameter space. We have experimented with various parameter combinations, but this study will use fixed values of a (28 K) and ϕ_0 (10°)—which approximate Earth's climate—and focus on varying SST gradients (b = 0.3, 0.5,. . . , 3.0, 4.0). The experimented profiles range from nearly globally homogeneous (b = 0.3) to sharp gradients in the subtropics (b = 4.0), effectively bridging and extending two classes of profiles that were widely used in idealized simulations (i.e., globally homogeneous profiles and present-climate profiles). Furthermore, these profiles are approximately consistent with paleoclimate records, which suggest the differences between the past and the present SSTs are relatively small in the tropics but can reach ±10 K in the extratropics (e.g., Annan and Hargreaves 2013; Naafs et al. 2018). An example of the prescribed SSTs with b = 0.85 is available in Fig. 2a. Section 3 will discuss the experiments with different SST profiles in detail.

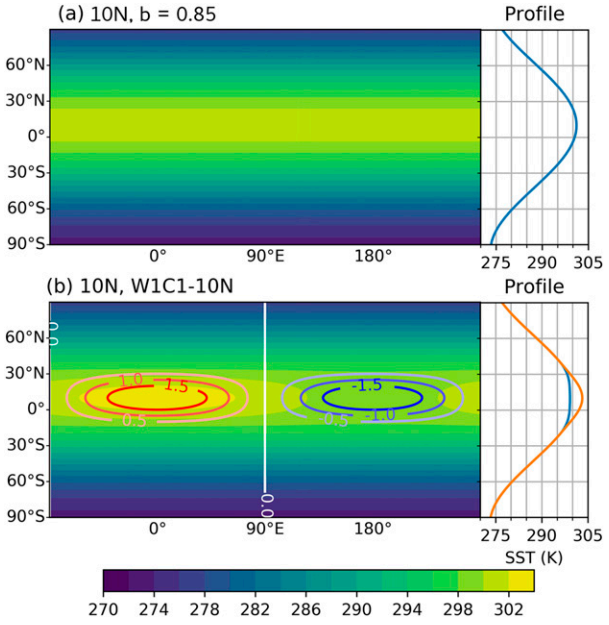

FIG. 2. (left) Examples of (a) zonally symmetric (b = 0.85) and (b) zonally asymmetric (W1C1–10N) SST forcings used in aquaplanet experiments. Color shading in (a) and (b) shows the values of prescribed SSTs (K). Contours in (b) show the wavenumber-1 perturbations centered at 10°N. (right) The meridional SST profile at (a) 0° and (b) 0° and 180°.

In our zonally asymmetric experiments, we combine the SST function from Eq. (1) with zonally varying perturbations in the following form:

$$\Delta T(\phi,\lambda) = \begin{cases} X\cos\left(\frac{\pi N\lambda}{180}\right)\cos^2\left[\frac{\pi(\phi-\phi_1)}{2W}\right], & \phi_1 - W \le \phi \le \phi_1 + W \\ 0, & \text{else} \end{cases}, \tag{2}$$

where ΔT (K) is a function of latitude ϕ (−90° to +90°) and longitude λ (0° to 360°), X (K) is the maximum magnitude of zonally asymmetric perturbations, N is a parameter that sets the wavenumber of SST perturbations, W modifies the meridional extent of the zonally asymmetric perturbations, and ϕ_1 (°) is the latitude where the maximum of these SST perturbations appears. The function is similar to those used by Neale and Hoskins (2000; "3KW1 experiment") and some recent monsoon-like simulations (Wu and Shaw 2016). This study primarily discusses experiments with zonal wavenumber-1 perturbations that maximize at 2 K and extend 60° of latitude (X = 2 K, N = 1, and W = 30°). Furthermore, we compare model responses to combinations of warm-cold perturbations ("W1C1") and warm perturbations only ("W1C0") to illustrate the impacts of local and remote SSTs. Different from some earlier studies that explore TC activity with zonally asymmetric SST forcings (Ballinger 2015; Defforge 2016), we investigate the effects of positioning SST perturbations at different latitudes (0°–30°N). This approach is a stepping stone for idealized studies of how equatorial and meridional ocean modes affect TC activity. Figure 2b provides an example of the SST function with the W1C1 pattern centered at 10°N. The experiments with these zonally asymmetric SST patterns will be further discussed in section 4.

c. TC tracking

To identify and track simulated TCs, this study uses the GFDL vortex tracker that has been documented in detail by

Zhao et al. (2009). In short, the tracker identifies candidate warm-core vortices using 6-hourly instantaneous 850-hPa relative vorticity, sea level pressure, and upper-tropospheric temperature anomalies. The threshold values used in this vortex search are identical to those used by Zhao et al. (2009). Once a coherent warm-core vortex is identified, the maximum near-surface wind speed near the vortex centers is recorded on a 6-hourly basis. The tracker then links these warm-core vortices to the vortices that are within 400 km at the previous time step. To qualify as a TC, for at least 3 days during the life of a tracked vortex, its intensity should reach tropical storm wind strength, though not necessarily on consecutive days. For simplicity, we denote the first and the last warm-core vortex records identified by the TC tracker as genesis and lysis points, respectively. Composite analyses of the identified storms show TC-like structures along with some intensity biases. The results from a storm-rich experiment ($b = 0.3$) are available in the appendix (Figs. A1 and A2).

3. Simulations with zonally symmetric settings

a. Simulated weather and climate equilibria

To help with the interpretation of simulations, we first examine two simulations with extremely strong ($b = 4.0$) and extremely weak ($b = 0.3$) meridional SST gradients. Figures 3a and 3c show the precipitation during the first six hours of Day 182, respectively. The atmospheres in the two simulations are in different dynamic regimes. With strong SST gradients ($b = 4.0$), the ITCZ is well defined and located near 10°N (i.e., the latitude of maximum SST). Furthermore, some precipitation bands extend from the ITCZ and reach the midlatitude, resembling the atmospheric rivers in Earth's present-day climate. These precipitation bands are directly related to baroclinic waves, which contribute to notable synoptic variability at the tropical–extratropical interface and readily absorb convective disturbances that develop from the ITCZ.

The simulation with weak SST gradients ($b = 0.3$) lacks a well-defined ITCZ. Instead, the equatorial precipitation appears in a wavenumber-1 envelope that propagates eastward with a period of 50–60 days. To some extent, the global-scale envelope resembles the Madden–Julian oscillation (MJO) (Zhang 2005). At higher latitudes, the model domain is filled with vortices that have intense precipitation. A composite analysis of these vortices shows TC-like warm-core structure (Fig. A1) despite their unusual genesis latitudes. The vortex-rich regime resembles the global-scale simulations of rotating radiation-convection equilibrium (RCE) forced with homogeneous SST (e.g., Shi and Bretherton 2014; Merlis et al. 2016; Chavas and Reed 2019). Perhaps surprisingly, an RCE-like state can exist even when SST gradients are present—provided that the subcloud layer moist entropy is relatively homogeneous and helps to avoid a strong large-scale overturning circulation (Emanuel 1995; Singh et al. 2017; also see Fig. 7j). While these weather perturbations and the MJO-like feature are interesting, the rest of this section will mostly address TC-related climate features and statistics of the equilibrated climate.

To show that the above snapshots are representative of the equilibrated climates, we examine the 2-yr evolution of precipitation and precipitable water between ~10°S and ~30°N (Figs. 3b,d). This region centers on the latitude with the SST maximum, and small changes of the latitude range do not qualitatively alter the results to be presented. In both simulations, the tropical climate reaches equilibrium after the first 90 days. This equilibration time scale is similar to that in aquaplanet experiments forced with globally homogeneous SST (Chavas and Reed 2019). Given this fast equilibration, we analyze the simulated climates using data between day 182 and day 731. The tropical precipitation has strong intraseasonal variability when the meridional gradient of SSTs is weak (Fig. 3d). However, the simulation's precipitation within the examined tropical domain is weaker by ~1.5 mm day^{-1} than that in the simulation with strong SST gradients, even though the latter has substantially lower precipitable water (<25 mm; Fig. 3b). The climates in Fig. 3 represent the two extreme ends simulated with our zonally symmetric forcings.

b. Characteristics of large-scale environment and TC activity

The variations of the meridional gradient of SSTs strongly affect global TC number and distribution (Fig. 4). When the SST gradient reduces (from $b = 4.0$ to $b = 0.3$; see Fig. 5a for details), the TC genesis number between the equator and 70°N increase by two orders of magnitude. From $b = 4.0$ to $b = 1.0$, the increase of TC genesis is mostly concentrated between 10° and 30°N. From $b = 0.85$ to $b = 0.3$, the genesis increase is ~150% and mostly occurs poleward of 30°N. Meanwhile, the increase of TC track density occurs in a similar way (not shown). It is also noticeable that some TCs (i.e., warm-core storms) form at relatively low SSTs (<295 K) in the intermediate regimes (e.g., Figs. 4f,g), consistent with the fact that some TCs form at low SSTs in Earth's present climate (e.g., McTaggart-Cowan et al. 2015) and some climate simulations (Sugi et al. 2015). These high-latitude genesis events may not be well constrained by empirical indices of genesis potential, which are usually devised based on low-latitude events of the present climate (e.g., Camargo et al. 2007). Figure 4 also suggests that unforced variability contributes to some zonal variations of TC genesis. As an example of unforced noise, the TC genesis number in the sectors of 270°−0°–90°E and 90°−180°–270°E differ by 24 in the $b = 1.5$ experiments. But excluding the experiments with few TC genesis (Figs. 4a,b), these zonal variations are at least one order of magnitude smaller than the local climatological values.

Figure 5 shows the zonal averages of the large-scale environment and TC genesis numbers. The SST profile with $b = 1.0$ is close to the Northern Hemisphere summer of Earth's present climate, while the profile with $b = 0.3$ is nearly globally homogeneous. When b varies between 4.0 and 2.0, the maxima of precipitable water, precipitation, and maximum potential intensity (MPI; Emanuel 1988) are located near 10°N, approximately corresponding to the maximum of the prescribed SSTs. In these individual experiments, the transition from low-latitude maxima to high-latitude low values is mostly smooth. An exception is the MPI in the subtropics, which shows some

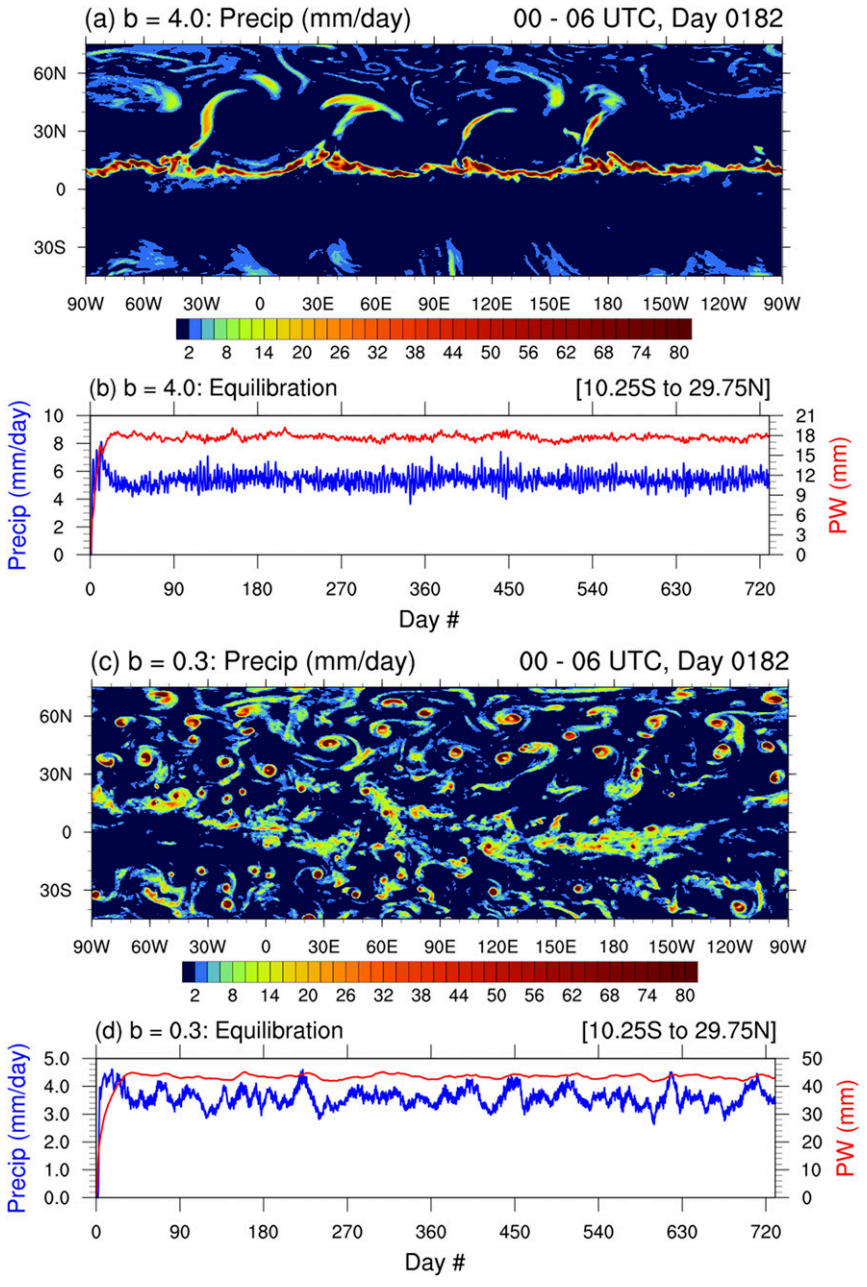

FIG. 3. Precipitation snapshots and tropical equilibration in two zonally symmetric experiments. The two experiments are (a),(b) $b = 4.0$ and (c),(d) $b = 0.3$. (a) Precipitation rate (mm day^{-1}) averaged between 0000 and 0600 UTC of the 182nd day of simulation. (b) The 2-yr evolution of precipitation rate (blue; mm day^{-1}) and precipitable water (red; mm) averaged between about 10°S and 30°N. Small changes in the latitude range do not change the results qualitatively. The plotting settings of (c) and (d) are as in (a) and (b).

sharp transitions because the official MPI calculation code[1] imposes numeric constraints on systems with relatively high pressure and weak wind. As the SST gradient further reduces from $b = 2.0$, the maxima of precipitation gradually weaken and shift equatorward—before eventually flattening out ($b = 0.3$). We consider the precipitation maxima as the ITCZ latitude and note that it tends to appear near or slightly equatorward of the SST maxima (Privé and Plumb 2007). When a well-defined ITCZ is present ($b = 4.0 \rightarrow 1.0$), its northern flank is characterized by a local minimum of the vertical wind shear, which we define as the magnitude of the wind vector difference

[1] ftp://texmex.mit.edu/pub/emanuel/TCMAX/.

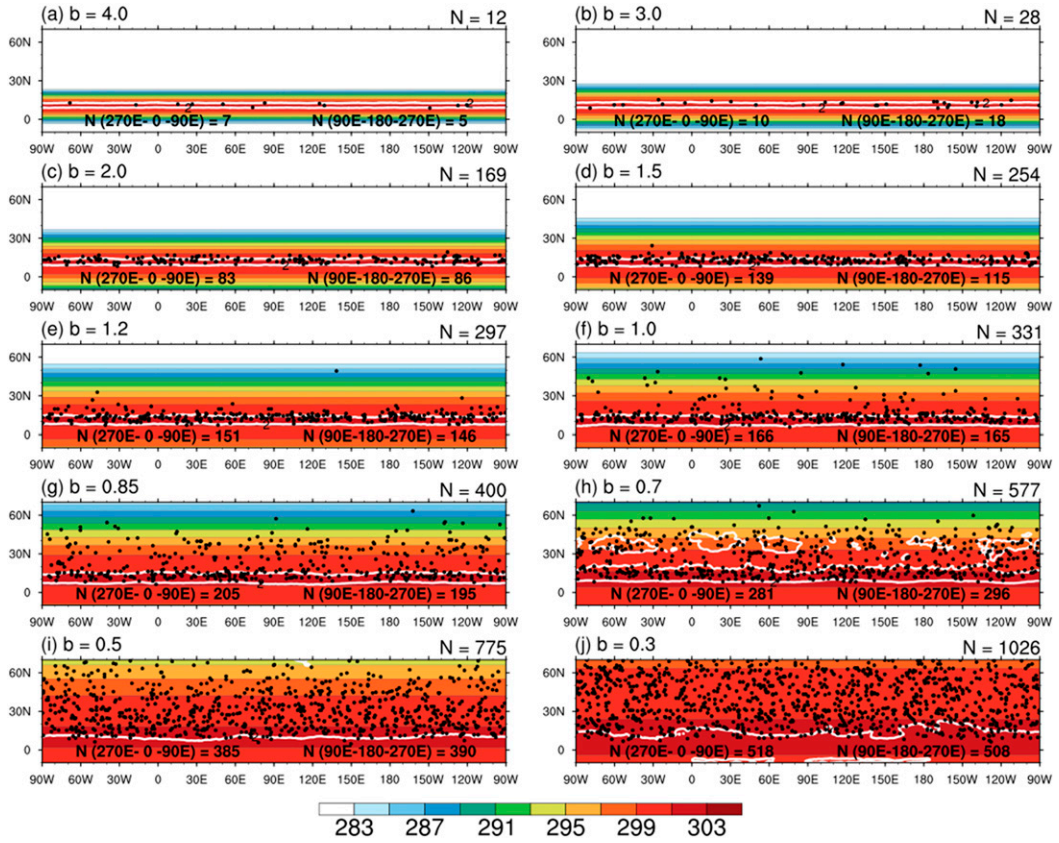

FIG. 4. Simulated TC genesis and the associated zonally symmetric SST forcings (K; shading). (a)–(j) The experiments with $b = 4.0, 3.0, \ldots, 0.5$, and 0.3, respectively, as noted in the upper-left corner of each panel. Black dots denote the genesis location during a 1.5-yr period. The white contours show the dimensionless genesis potential index (GPI; Camargo et al. 2007), and the only plotted level is GPI = 2. The total number of TCs that form between the equator and 70°N is denoted in the upper-right corner of each panel. The TC genesis number in the sectors of 270°–0°–90°E and 90°–180°–270°E is denoted at the bottom of each panel.

between 200 and 850 hPa. The north flank region also has relatively strong low-level vorticity, which is related to the low-level convergence and stretching effect of frequent convective heating (Ferreira and Schubert 1997; Wang and Magnusdottir 2005). Consistent with these favorable environmental factors, TC genesis between 5° and 20°N remain relatively active within these simulations ($b = 4.0 \rightarrow 0.70$). This genesis maximum does not shift with the precipitation and appears anchored by relatively weak vertical wind shear and strong low-level vorticity. Furthermore, this genesis maximum in most experiments can be *qualitatively* captured by the genesis potential index[2] (GPI; Camargo et al. 2007). However, a comparison among experiments suggests some limitations related to GPI's quantitative aspect. For example, the highest GPI value between 5° and 15°N appears in the experiment with $b = 4.0$, but the simulated genesis in this experiment is the lowest among all the experiments.

Figure 5 also reveals an interesting increase of high-latitude genesis when the meridional gradients of SST are relatively weak ($b = 1.0 \rightarrow 0.3$). A composite analysis of these storms shows TC-like warm-core structure (Fig. A1) despite their unusual genesis latitudes and some structural differences relative to the low-latitude storms. The increase of these genesis events is consistent with the increase of SST and precipitable water, as well as relatively low values of the vertical wind shear in the midlatitudes. While the MPI forbids TC activity when the extratropical SST is extremely low, it is clear that the MPI values are high enough to support at least low-intensity TCs at 50°N—even for the experiment with the lowest extratropical SST under consideration ($b = 1.0$). Therefore, the MPI itself does not appear to be the leading constraint of the high-latitude genesis for $b = 1.0 \rightarrow 0.3$. The GPI changes appear qualitatively consistent with genesis changes, even though this metric overestimates high-latitude genesis while underestimating low-latitude genesis in the experiment with $b = 0.3$. We also note that an increase of genesis in the extratropics also

[2] The GPI formulation in this study follows Camargo et al. (2007): $\text{GPI} = |10^5\eta|^{3/2}(\text{RH}_{600}/50)^3(\text{MPI}/70)^3(1 + \text{VWS}/10)^{-2}$, where η is the 850-hPa absolute vorticity, RH_{600} is the 600-hPa relative humidity, MPI is the maximum potential intensity, and VWS is the 200–850-hPa vertical wind shear.

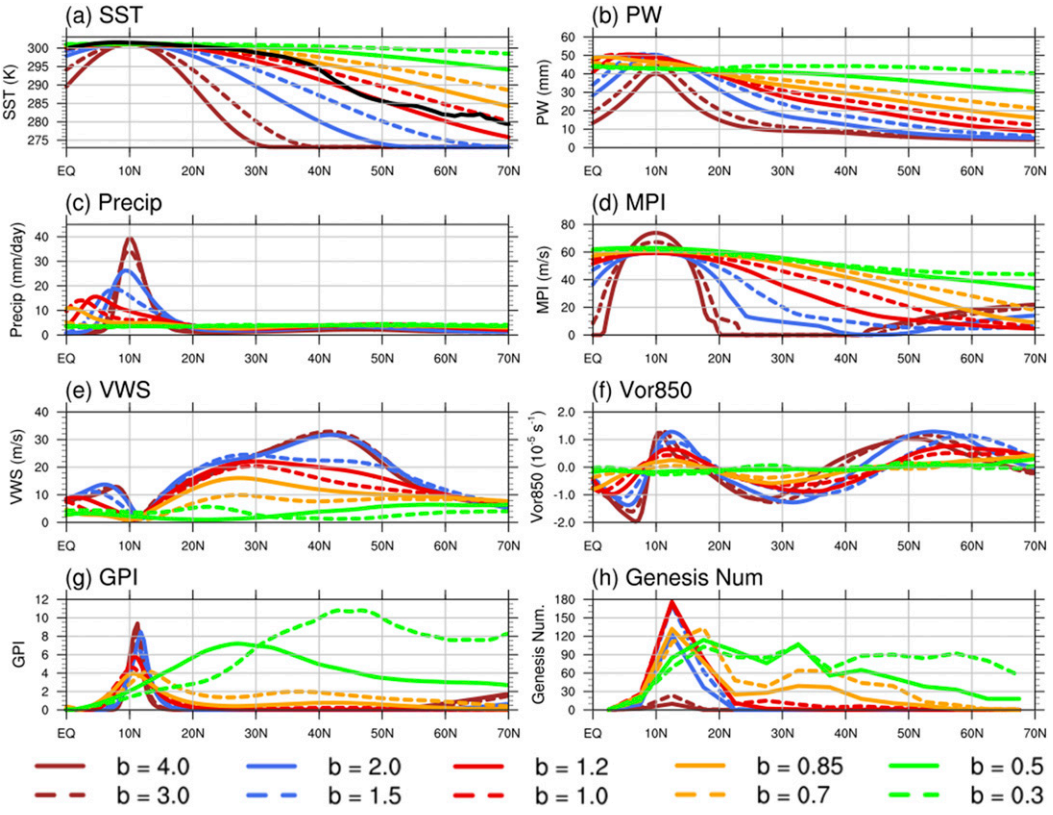

FIG. 5. Zonal averages of environmental variables and TC genesis number in the experiments with zonally symmetric SSTs (maxima at 10°N). (a) SST (K), (b) precipitable water (mm), (c) precipitation (mm day^{-1}), (d) maximum potential intensity (m s^{-1}), (e) vertical wind shear (m s^{-1}), (f) 850-hPa relative vorticity (s^{-1}), (g) genesis potential index (unitless), and (h) genesis number in 5° bins of latitude. The line legends that denote the experiments are at the bottom. Black line in (a) shows the zonal average of July–August SST (1979–2013) from HadISST (Rayner et al. 2003).

appears when the SST warms uniformly in aquaplanet simulations (Merlis et al. 2016) and when CO_2-related warming is included in atmospheric GCM simulations with more realistic settings (Yoshida et al. 2017).

The circulation and genesis responses to the reduction of meridional SST gradients are qualitatively consistent with Fedorov et al. (2019), who used a different model and somewhat similar SST profiles. With off-equator SST maxima, Fedorov et al. (2019) found that a reduction of the tropics-to-pole SST differences weakens the ITCZ precipitation and shifts it equatorward in their hypo-hydrostatic simulations. The consistency suggests the relationship between the ITCZ and the meridional gradient of SST is qualitatively robust. Interestingly, a poleward migration of TC activity with the reduction of meridional SST gradient also appears in the hypo-hydrostatic simulations by Fedorov et al. (2019). However, their simulations produce a clear subtropical ''desert'' that separates the tropical and midlatitude maxima of TC genesis, while AM4.0-Aqua simulations ($b = 0.7, 0.85$) produce smoother latitudinal variations of TC genesis. The reasons for this inconsistency between their hypo-hydrostatic simulations and our AM4.0-Aqua simulations is not clear.

We can further examine the simulated TC activity using a two-dimensional probability distribution function (PDF) of the lifetime maximum intensity (LMI) and the latitudes where the LMI is attained[3] (Fig. 6). With a reduction of the meridional SST gradient, the PDFs show a poleward migration of the LMI latitudes from the tropics to higher latitudes. Interestingly, the poleward migration is rather evident when the SST profiles vary near $b = 1.0$, which roughly corresponds to the zonal average of SST in Earth's present climate (Fig. 5a). Besides the poleward migration, the mean LMI values also increase by ~ 2 m s^{-1} between the experiments with $b = 4.0$ and $b = 0.3$. The LMI increase with the reduction of SST gradients occurs partly because the lifetime of TCs increases significantly (Table 2), which indicates that TCs spend a longer time developing over warm SSTs in the experiments with small b values. Nonetheless, the intensity of simulated TCs is generally below the MPI, suggesting that TC intensification is also constrained by other processes. The results are qualitatively

[3] If the LMI value of a TC is reached more than once, then the calculation considers only the first time when the TC attains its LMI.

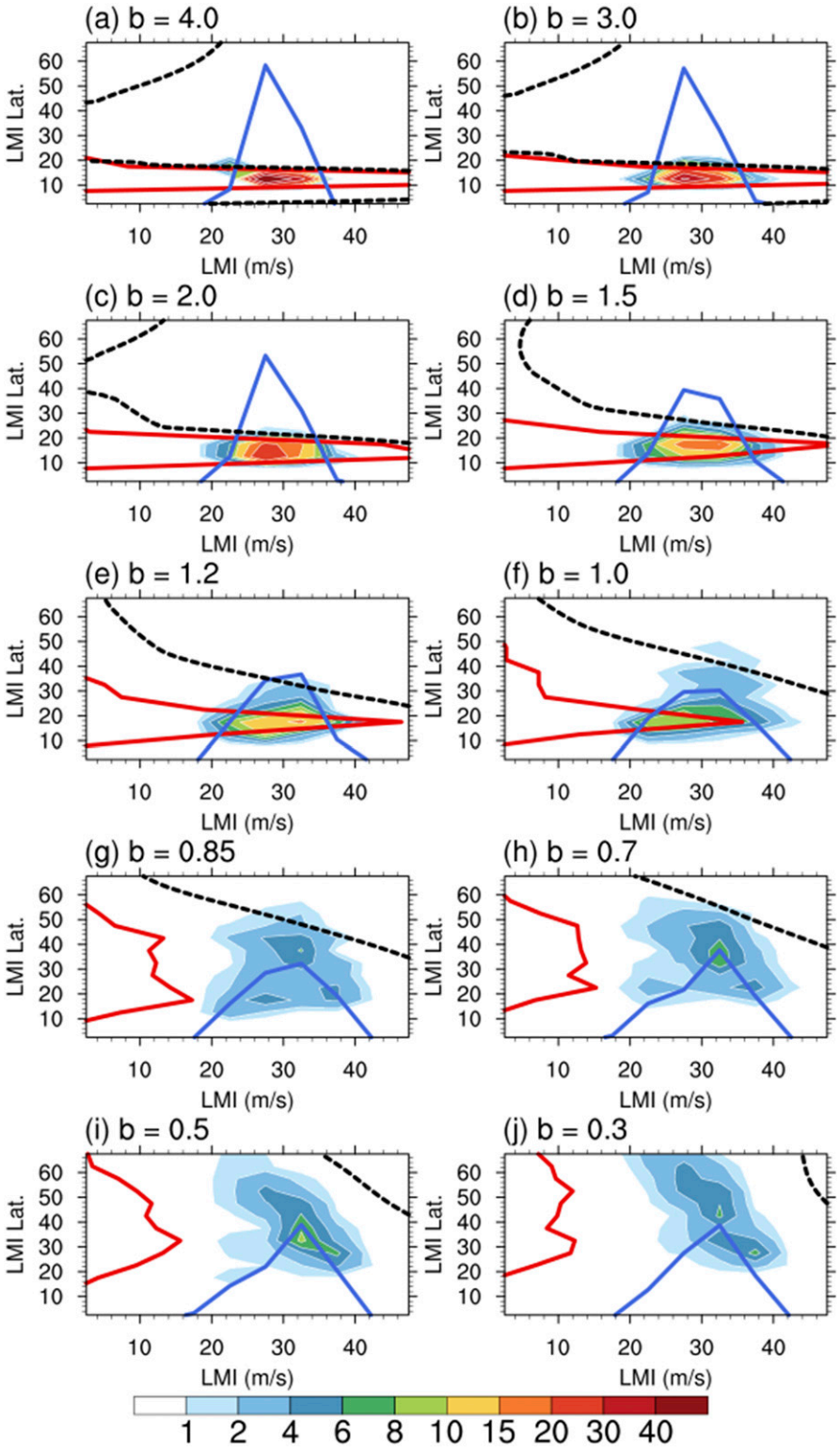

FIG. 6. Two-dimensional probability distribution function (%; shading) of the lifetime maximum intensity (LMI; $m\,s^{-1}$) and the latitudes where the LMI (°N) is achieved. The LMI is determined by searching the maximum of near-surface wind speed in the life cycle of individual storms. (a)–(j) The experiments with $b = 4.0, 3.0, \ldots, 0.5$, and 0.3, respectively, as noted in the upper-left corner of each panel. The blue and red curves show the probability distribution functions of LMI (x axis) and LMI latitudes (y axis), respectively. The percentage values correspond to the values on the perpendicular axes. The black dashed lines show the maximum potential intensity ($m\,s^{-1}$) as a function of latitudes.

TABLE 2. Indices of tropical circulation and TC activity. The ITCZ latitude is the latitude where the maximum of tropical precipitation (>5 mm day^{-1}, between 30°S and 30°N) is located. The ITCZ precipitation is the value of the identified precipitation maximum. The Hadley circulation edge is the latitude where the zero contour of the vertically averaged (300–700 hPa) meridional streamfunction is located. TC number is the counts of storms identified using the tracking algorithm. Genesis near ITCZ is the number of genesis that occur ±10° of the ITCZ latitude. The values of the three remaining TC indices are the averages of the storms that form between the equator and 70°N, followed by "±" and standard deviations among storms. The "N/A" note in the circulation columns indicates that the identification is not robust due to the very weak tropical overturning circulation. The arrows in the last row summarize the changes of metrics with the decrease of meridional SST gradients, which include monotonic decrease (↓), mostly increase (↗), and monotonic increase (↑).

b value	ITCZ lat (°N)	ITCZ precip (mm day^{-1})	HC edge (°N)	TC number	Genesis near ITCZ	Genesis lat (°N)	LMI lat (°N)	TC lifetime (h)
4	10	39	27	12	12	11 ± 1	13 ± 1	87 ± 23
3	10	34	28	28	28	12 ± 2	14 ± 2	89 ± 31
2	9	26	30	169	169	13 ± 2	15 ± 2	107 ± 33
1.5	8	19	32	254	243	13 ± 2	17 ± 4	132 ± 57
1.2	5	16	32	297	199	14 ± 4	19 ± 6	147 ± 72
1	2	14	32	331	127	16 ± 9	23 ± 10	165 ± 84
0.85	0	11	31	400	31	22 ± 12	31 ± 12	180 ± 94
0.7	−4	8	33	577	0	26 ± 13	36 ± 12	205 ± 106
0.5	N/A	N/A	N/A	775	N/A	31 ± 15	39 ± 13	230 ± 127
0.3	N/A	N/A	N/A	1026	N/A	38 ± 17	44 ± 14	256 ± 162
Summary	↓	↓	↗	↑	N/A	↑	↑	↑

similar if one considers only TCs that form between the equator and 40°N or uses the minimum sea level pressure in the LMI analysis (not shown). Last, the model physics and spatial resolution used in this study produce a biased wind–pressure relationship (Fig. A2) and cannot simulate strong wind associated with intense TCs (Fig. 6; Zhao et al. 2018a,b; Davis 2018). These issues might contribute an underestimate of intense TCs' sensitivity to the meridional SST gradients.

c. Links between the Hadley circulation and TC activity

We now examine the large-scale circulation simulated with the zonally symmetric forcings (Fig. 7). The meridional streamfunction shows that the winter Hadley cell is notably stronger than its summer counterpart. Both cells of the Hadley circulation weaken with a reduction of the meridional SST gradient, qualitatively consistent with the sensitivity indicated by a scaling analysis and global climate models (Seo et al. 2014; Shi and Bretherton 2014; Singh et al. 2017). Meanwhile, the meridional gradients of streamfunction also indicate that the ITCZ-related ascent shifts southward and weakens (b = 4.0 → 0.70), consistent with the findings in section 3b. Although the weakening and contracting features of the winter cell are striking, hereafter we focus on the summer cell and ITCZ as their changes have interesting and more direct implications for TC activity. For example, the summer-hemisphere Hadley cell becomes weak and ill-defined as the SST gradient reduces relative to an Earth-like profile (b = 1.0). In these circumstances, the summer Hadley cell—especially the proportion poleward of the ITCZ—may be too weak to effectively constrain TC activity.

Table 2 presents the metrics involving the relationships of the Hadley circulation and TC activity that were proposed by earlier studies (section 1). We first examine the ascent branch of the Hadley circulation, namely the ITCZ. As suggested in the discussion of Fig. 5, the global TC number in our simulations (b = 4.0 → 0.70) is associated with the latitude and the intensity of the ITCZ, but the associations manifest as statistically significant *negative* correlations (r = −0.95 and −0.96, respectively). The results are similar if streamfunction extrema are used to characterize the strength of the Hadley circulation (not shown). The relationship appears opposite to the positive correlations identified by earlier model studies (Merlis et al. 2013; Ballinger et al. 2015) and observational analysis (Zhang and Wang 2013, 2015). Nonetheless, the differences are mainly related to the TCs that form at relatively high latitudes, which only occur occasionally in Earth's present climate but account for a majority of global TCs as the meridional gradient of SST decreases (b = 1.0 → 0.3). If one focuses on TCs that form *near* the ITCZ latitude (±10°; Table 2) and compares the experiments with SST profiles near Earth's present climate (b = 1.5 → 0.7), the correlations between the ITCZ latitude/intensity and the TC genesis number become positive and thus consistent with the earlier studies (Merlis et al. 2013; Ballinger et al. 2015; Zhang and Wang 2013, 2015). The near-ITCZ genesis is similar to the ITCZ breakdown process in the real world (e.g., Wang and Magnusdottir 2005, 2006); the physical processes that contribute to these genesis events will be reported in a separate study. Last, it is worth noting that our AM4.0-Aqua simulations use prescribed SST, but Merlis et al. (2013) and Ballinger et al. (2015) used an earlier GFDL model with the slab-ocean setting. We caution that neither our nor the earlier findings should be extended beyond the original experimental contexts.

We now consider the relationships between the poleward edge of the Hadley circulation and TC activity (Table 2). The reduction of the SST gradient leads to a moderate expansion of the summer Hadley cell—the distance between its poleward edge and the ITCZ—as expected with a scaling analysis based on the eddy momentum budget and the baroclinic instability (Kang and Lu 2012). Across our experiments, the expansion of summer Hadley cell is mostly contributed by the equatorward shift of the ITCZ; the poleward edge shifts slightly poleward

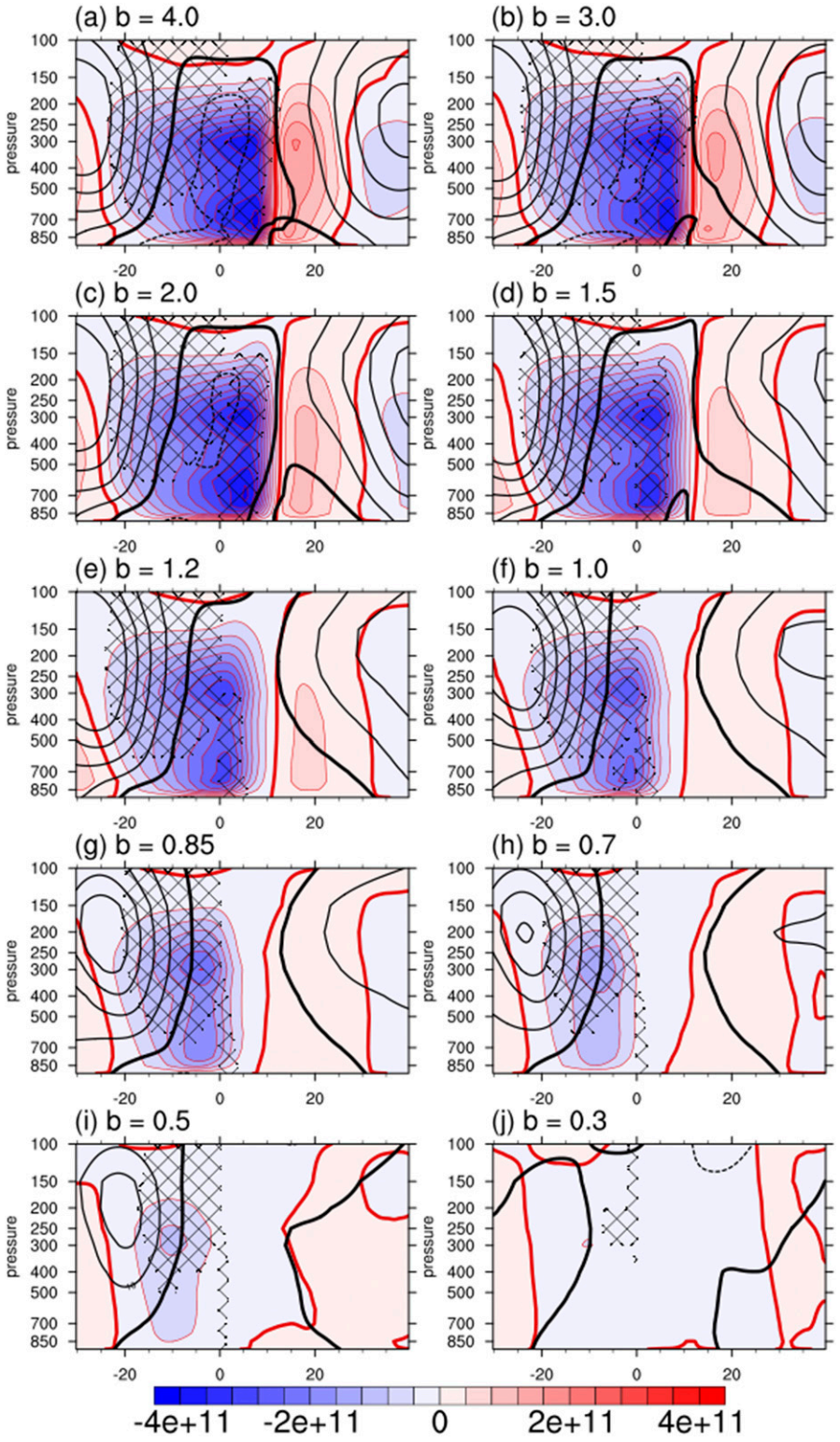

FIG. 7. Zonal averages of the large-scale circulation in the simulations forced by zonally symmetric SSTs. (a)–(j) The experiments with $b = 4.0, 3.0, \ldots, 0.5$, and 0.3, respectively, as noted in the upper-left corner of each panel. Color shading with red contours shows the meridional streamfunction ($\mathrm{kg\,s^{-1}}$; Oort and Yienger 1996). The negative values indicating counterclockwise overturning circulation, and the zero contours used to define the Hadley circulation edge are thickened. Black contours show the zonal wind ($\mathrm{m\,s^{-1}}$). Hatching denotes the regions subject to weaker eddy influences (Ro > 0.5).

when the meridional SST gradient is strong ($b = 4.0 \rightarrow 1.5$) but remains nearly constant thereafter (Table 2). The overall expansion of summer Hadley cell is accompanied by a poleward migration of the genesis latitude and the LMI latitude of TCs (Table 2), *qualitatively* consistent with the relationship identified using observational data (Kossin et al. 2014; Daloz and Camargo 2018; Studholme and Gulev 2018; Sharmila and Walsh 2018). But for experiments of $b = 4.0 \rightarrow 0.70$ ($N = 8$), the correlations between the Hadley circulation edge and the latitudes of genesis/LMI are only 0.62 and 0.67, respectively. Both correlations fail to reach the 95% confidence level, and the positive correlations do not hold well in the range of $b = 1.5 \rightarrow 0.7$. The results indicate that the summer cell of the Hadley circulation does not effectively constrain the latitudes of TC genesis or LMI, especially when the SST profiles vary near $b = 1.0$.

d. Constraint of baroclinic processes on TC activity

The weak constraint on the latitudes of TC genesis and LMI by the summer Hadley cell indicates an influence by other processes. In contrast to the winter Hadley cell, the summer Hadley cell is strongly mediated by extratropical eddies (Walker and Schneider 2006; Caballero 2007; Kang and Lu 2012). The importance of the extratropical effects in the momentum balance of the upper troposphere can be illustrated using a local Rossby number (Ro):

$$\mathrm{Ro} = -\frac{\zeta}{f}, \tag{3}$$

where ζ is the zonal mean of relative vorticity, and f is planetary vorticity. This nondimensional metric characterizes the zonal momentum balance of the mean circulation, as well as the relative importance of the thermally driven and the eddy-driven components of the mean circulation (Walker and Schneider 2006). Ro $\rightarrow$ 0 suggests that the mean circulation is directly coupled with the eddy momentum flux, which is generally the case for the simulated summer Hadley cell (Fig. 7). The scaling does not indicate causality, but it does suggest that changes in the summer Hadley cell are intrinsically connected to changes in eddy activity. Based on our observation of synoptic processes in AM4.0-Aqua simulations and empirical knowledge of simulated and real-world TC activity (Zhang et al. 2016, 2017, 2019), we hypothesize that the latitude changes of TC genesis and LMI are influenced by extratropical eddy activity.

In the simulations with a well-defined midlatitude jet in the summer hemisphere (Fig. 7), extratropical eddy activity primarily manifests as baroclinic waves. An example of these baroclinic waves has been presented in Fig. 3a, where developing baroclinic waves disrupt tropical disturbances, drive moisture plumes outside the tropics, and contribute to band-like precipitation in warm conveyor belts and midlatitude fronts. Since these baroclinic waves are accompanied by temperature advection, the wave activity can be approximated by daily variations of 500-hPa geopotential height (Fig. 8a). As the meridional gradient of SST reduces ($b = 4.0 \rightarrow 0.3$), the geopotential height variations weaken in the midlatitudes and shift poleward. The weakening is also evident for the 200-hPa zonal

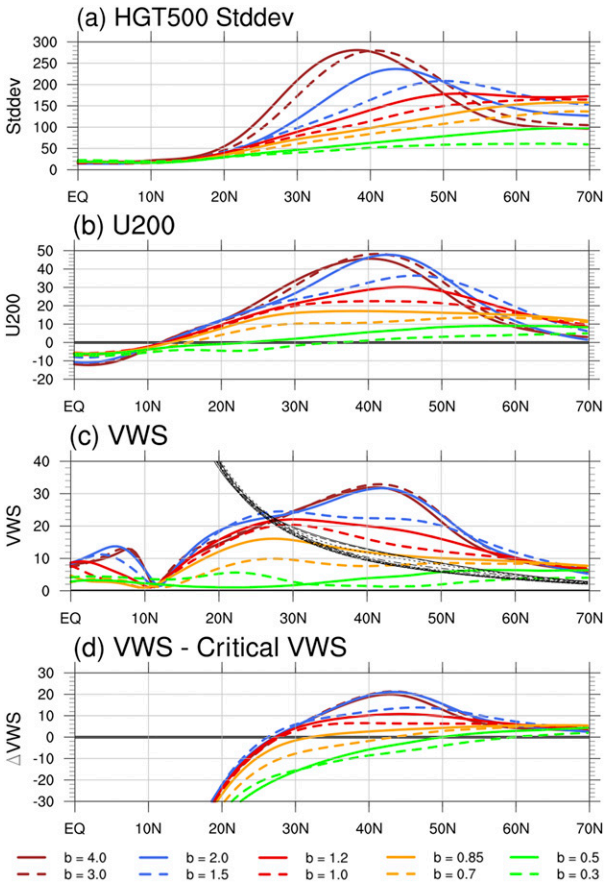

FIG. 8. Zonal-mean metrics of extratropical eddy activity and baroclinic environment. (a) Standard deviations of 500-hPa geopotential height (m), calculated using daily data during a 1.5-yr period, (b) 200-hPa zonal wind ($\mathrm{m\,s^{-1}}$), (c) vertical wind shear ($\mathrm{m\,s^{-1}}$), and (d) vertical wind shear minus the critical wind shear of environmental baroclinic instability. The black lines in (c) show the envelope of the critical wind shear values from all the experiments. The black line in (d) highlights the zero value.

wind (Fig. 8b), even though the poleward shift of the midlatitude jet is ambiguous as the jet becomes ill-defined with small b values. In particular, the absence of a sharp and narrow jet with $b = 1.0$ differs from the real world and is likely related to the locally enhanced meridional SST gradient near 45°N (Fig. 5a).

The poleward shift of baroclinic wave activity can be characterized by a critical condition for baroclinic instability (Vallis 2017):

$$\mathrm{VWS}_c = \frac{\beta H^2}{4}\frac{N^2}{f^2}, \tag{4}$$

where VWS_c is the critical vertical wind shear for baroclinic instability, β is the meridional gradient of the Coriolis parameter, H is the troposphere depth, N is the Brunt–Väisälä frequency, and f is the Coriolis parameter. The critical condition is derived from two-layer quasigeostrophic model (Vallis 2017); the development of baroclinic waves is only possible when vertical wind shear is greater than VWS_c. Equation (4)

slightly differs from the original Eq. (9.122) by Vallis (2017) as we kept the unit of wind shear on the LHS. Here we use this critical condition in a semiquantitative way and evaluate the values on the RHS based on the 200–850-hPa layer in the model output.

Figure 8c shows VWS_c with the 200–850-hPa vertical wind shear in simulations. The VWS_c values slightly differ among simulations but are overall similar. Overall, VWS_c shows high values equatorward of 20°N at lower latitudes, suggesting that the tropics do not support baroclinic instability. At higher latitudes, VWS_c gradually decreases to $<5\ m\ s^{-1}$ and becomes comparable to the simulated vertical wind shear. Figure 8d shows their differences and the latitudes where these differences become zero (hereafter "critical latitude"). The critical latitudes remain near relatively constant for the experiments with $b = 4.0 \rightarrow 1.0$ (28°, 28°, 27°, 26°, 27°, 28°N) but rapidly shifts poleward as the meridional SST gradient further reduces (32°, 43°, 50°, 60°N). Even though some upper-level Rossby waves can propagate equatorward, this poleward shift of the critical latitude drives baroclinic wave activity to higher latitudes (Fig. 8a) and helps to free the midlatitudes from extratropical wave activity that is overall detrimental for TC development (e.g., Zhang et al. 2016, 2017). This conceptual picture appears consistent with the large increase of high-latitude TCs when the meridional SST gradient is relatively small ($b = 1.0 \rightarrow 0.3$). Furthermore, the critical latitude of VWS_c shows strong correlations with the latitudes of TC genesis ($r = 0.97$, $N = 10$) and LMI ($r = 0.92$, $N = 10$) and account for the simulations that have ill-defined summer Hadley cells ($b = 0.5 \rightarrow 0.3$).

To better understand the environmental constraints on the latitudes of TC genesis and LMI, we present their relationships with the Hadley circulation edge and VWS_c in Fig. 9. Consistent with earlier studies (Daloz and Camargo 2018; Studholme and Gulev 2018), the LMI latitudes strongly depend on the genesis latitudes ($r = 0.98$, $N = 10$) in all the simulations. When the meridional SST gradients and the summer Hadley cell are relatively strong ($b = 4.0, \ldots, 1.5$), the latitudes of TC genesis and LMI shift poleward with the Hadley circulation edge (Fig. 9a). However, this dependence breaks down when the meridional SST gradients and the summer Hadley cell are relatively weak ($b = 1.5 \rightarrow 0.3$). In this range, the latitudes of TC genesis and LMI shift poleward with the critical latitude of VWS_c (Fig. 9b). These results thus suggest the relative importance of Hadley circulation and baroclinic processes depends on climate states. Interestingly, baroclinic processes appear to be more important in the climate states simulated with Earth-like SST profiles ($b = 1.2 \rightarrow 0.85$). This finding suggests that future investigations of TC genesis/LMI latitudes should consider both tropical and extratropical processes.

Overall, the results in section 3c and section 3d suggest both tropical and extratropical processes modulate TC activity in the experiments with zonally symmetric forcings. We caution that our results should not be extended to the real world without further scrutiny, as zonally asymmetric SST and inhomogeneous lower boundary conditions (e.g., land and ocean) may introduce nontrivial complications, especially on the regional scale (e.g., Zhang and Wang 2019; Wang et al. 2020). Furthermore, greenhouse gas forcings may introduce additional complications (e.g., Merlis et al. 2013).

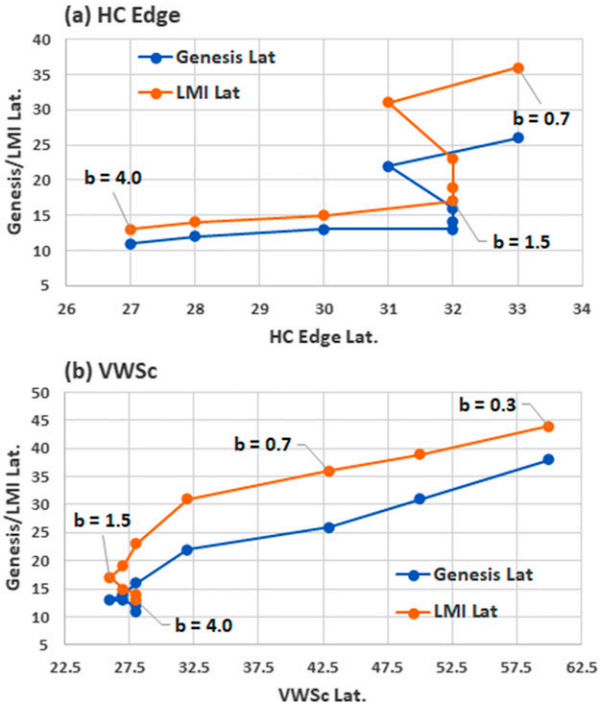

FIG. 9. Tropical and extratropical controls of the latitudes of TC genesis (blue) and LMI (orange). The plotted relationships are with (a) the polar edge of summer Hadley cell and (b) the critical latitude of VWS_c. In (a) only the results from the $b = 4.0 \rightarrow 0.7$ experiments are included as the Hadley circulation edge is not well defined in the other two experiments (Table 2). The lines connect data points following a specific order ($b = 4.0 \rightarrow 0.3$), and some key data points were labeled for clarity.

4. Simulations with zonally asymmetric settings

a. *Simulated weather and climate equilibria*

We proceed to the zonally asymmetric experiments with a reference simulation that has a relatively weak meridional SST gradient ($b = 0.85$). This choice is primarily motivated by the fact that the ITCZ in this simulation is located near the equator[4] and sensitive to SST perturbations (Fig. 5 and Table 2). The sensitivity makes it easier to perturb tropical precipitation and evaluate the CQE-WTG framework and the relative SST mechanism. This particular SST profile agrees well with the observations between the equator and 35°N (Fig. 5a). While the high-latitude part of this SST profile deviates from Earth's present climate, it corresponds to a climate with amplified polar warming and may resemble Earth's future

[4] Ballinger (2015) has documented TC activity in a series of aquaplanet experiments with an off-equator ITCZ and zonally asymmetric SST forcings.

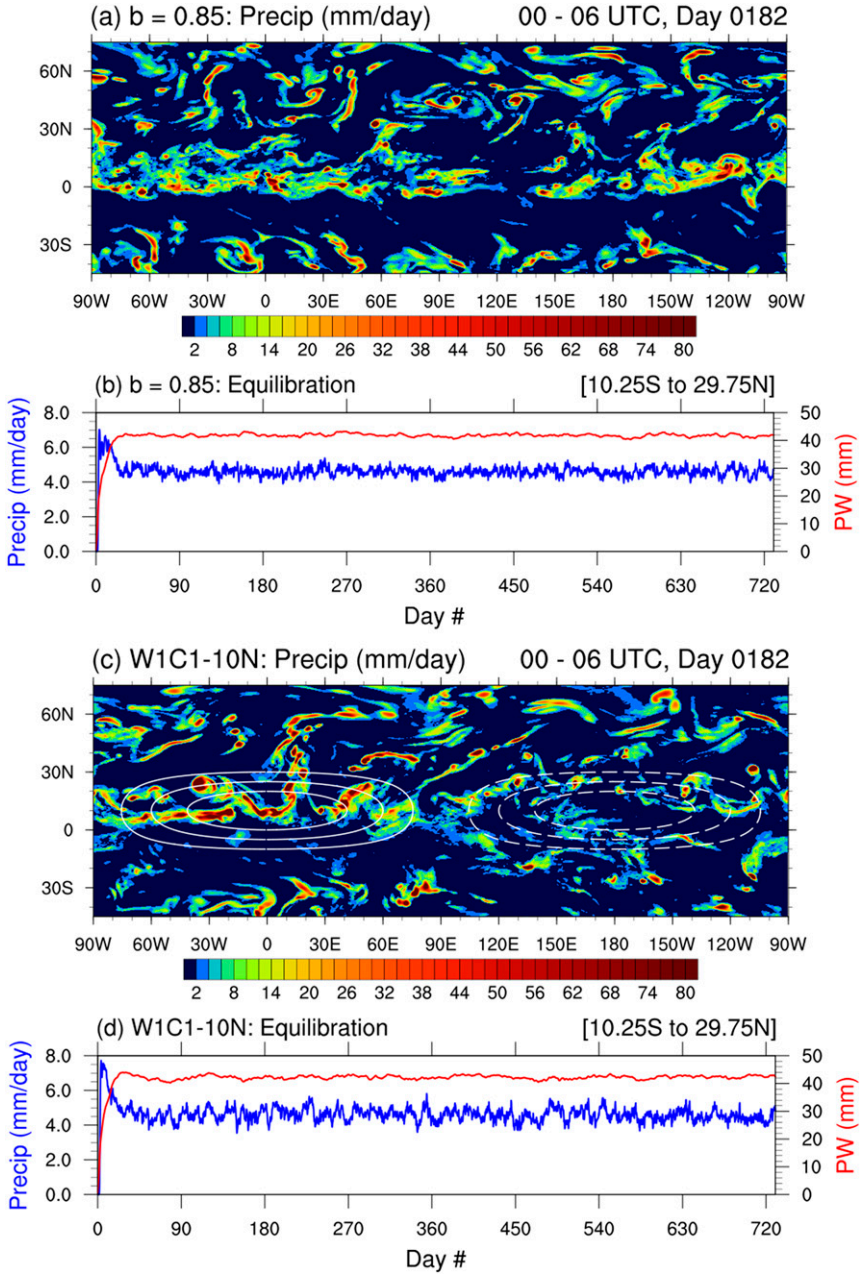

FIG. 10. Precipitation snapshots and tropical equilibration in two experiments with (a),(b) zonally symmetric forcings and (c),(d) zonally asymmetric forcings. The SST forcings in the two experiments are $b = 0.85$ (symmetric) and W1C1–10N (asymmetric). The asymmetric forcing is shown with white contours in (c). The solid and dashed contours show positive and negative values, respectively; the contour intervals are 0.5 K. The other plotting settings are as in Fig. 3.

climate. Furthermore, the relative abundance of TCs with $b = 0.85$ helps to highlight TC responses across a wide range of latitudes (Fig. 5h). The weather variations and climate equilibrium of this reference simulation ($b = 0.85$) are shown in Figs. 10a and 10b. Besides TCs, tropical cloud clusters, and moist baroclinic waves, the simulation also generates a planetary-scale and eastward-propagating envelope of tropical convective activity. This MJO-like mode contributes to spatiotemporal variations of tropical precipitation but is less striking than in the experiment with $b = 0.3$ (cf. Figs. 3c and 10a).

As an example of the zonally asymmetric experiments, Figs. 10c and 10d show the simulations with a zonal wavenumber-1 SST patch added to 10°N, namely ''W1C1-10N'' from Eq. (2). As expected, warm SST perturbations in 270°−0°–90°E (hereafter ''warm sector'') strengthen the local tropical

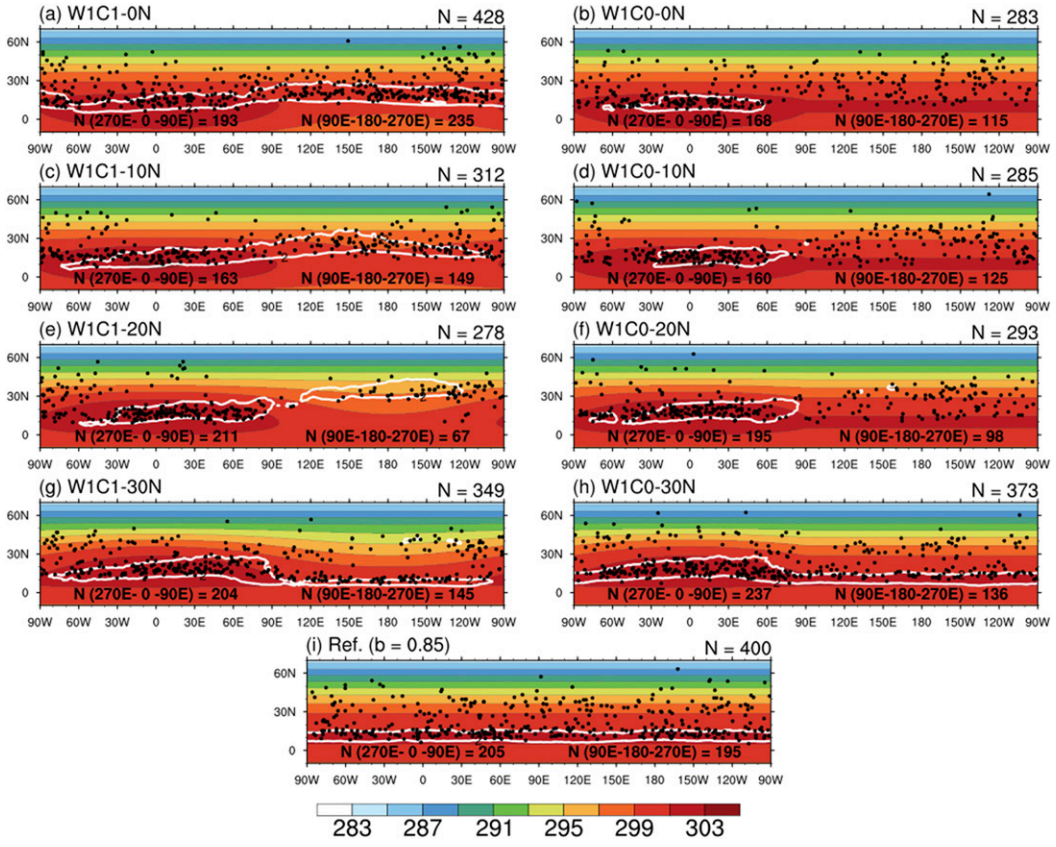

FIG. 11. Simulated TC genesis and the associated zonally asymmetric SST forcings (K; shading). (a)–(i) The experiments with W1C1–0N, W1C0–0N, . . . , W1C1–30N, W1C0–30N, and the zonally symmetric reference, respectively, as noted in the upper-left corner of each panel. The other plotting settings are as in Fig. 4.

precipitation. The precipitation mainly appears in the form of an ITCZ that breaks down and generates TCs. These cases of ITCZ breakdown and TC genesis are somewhat similar to those in the eastern Pacific (e.g., Hack et al. 1989; Ferreira and Schubert 1997; Wang and Magnusdottir 2005, 2006). In contrast, the sector with cold SST perturbations in 90°−180°–270°E (hereafter ''cold sector'') lacks a well-defined ITCZ, even though there are still some westward-moving features, which can be TCs or easterly waves that sometimes contribute to TC genesis. Figure 10d suggests that the addition of the zonal asymmetry does not strongly affect the time of equilibration or the tropical-mean moisture nor precipitation. However, this asymmetry seems to strengthen the temporal variability of area-mean (10°S–30°N) precipitation on the synoptic to monthly time scale (cf. Figs. 10b and 10d). As in section 3, the ensuing discussion will mainly address TC activity and the equilibrated climates.

b. *Characteristics of large-scale environment and TC activity*

Figure 11 shows the regional responses of TC activity to diverse asymmetric forcings (''W1C1'' and ''W1C0,'' see section 2b). We first consider TC activity in the sector with warm SST perturbations (270°−0°–90°E). Across all the experiments, a majority of TCs in the warm sector form around 15°N but not necessarily over the SST maximum (e.g., Fig. 11c with ''W1C1-10N''). These warm-sector TCs generally have higher wind speed and larger spatial size compared to those in the cold sector, which can be inferred from visual inspections of individual time steps (e.g., 25°N, 30°W vs 25°N, 130°E in Fig. 11c). The size differences suggest that SST patterns can add complexities to the TC size in aquaplanet simulations (Chavas and Reed 2019) and warrant future study. Depending on the SST perturbations, TC genesis number in the warm sector varies by as much as ~20% relative to the zonally symmetric reference simulation (b = 0.85), which generates 200 ± 5 TCs in the sectors of 270°–0°–90°E and 90°–180°–270°E (Fig. 11i). When the warm SST perturbations are centered at 10°N (Figs. 10c,d), the genesis number in the warm sector is nearly 20% lower relative to the reference, suggesting warm SST and vigorous convection by themselves do not necessarily increase TC genesis. The GPI captures some spatial characteristics of low-latitude TC genesis but does not always offer an accurate indication. For example, the ''W1C1-20N'' experiment shows relatively infrequent genesis in a high-GPI region (120°E–180°–120°W) and relatively frequent genesis in a low-GPI region (60°–120°W). The strength and shortcomings of the GPI (and a different genesis index) for interpreting idealized

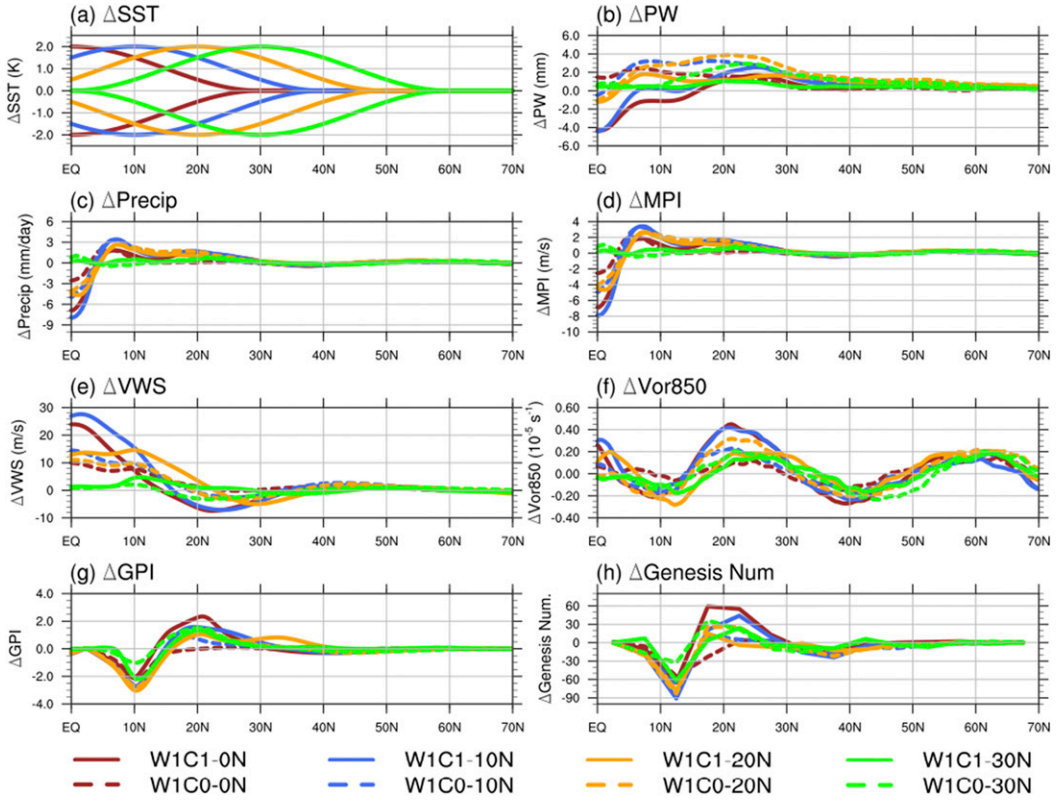

FIG. 12. Zonally averaged responses of environmental variables and TC genesis number to zonally asymmetric SST perturbations. The responses are defined as the differences from the reference experiment with zonally symmetric SSTs (b = 0.85, Fig. 5). (a) SST (K), (b) precipitable water (mm), (c) precipitation (mm day^{-1}), (d) maximum potential intensity (m s^{-1}), (e) vertical wind shear (m s^{-1}), (f) 850-hPa relative vorticity (s^{-1}), (g) genesis potential index (GPI), and (h) genesis number in 5° bins of latitude. The line legends that denote the experiments are at the bottom. The SST profiles in (a) show the values at the longitudes where maximum and minimum perturbations of W1C1 experiments are located; the SST profiles of the W1C0 experiments are omitted as their warm SST perturbations are identical to those of W1C1 experiments.

zonally asymmetric experiments have been examined extensively by earlier studies (Ballinger 2015; Frisius and Abdullah 2017). For brevity, here we refrain from elaborating on this topic.

The prescribed zonal asymmetry affects the zonal means of the large-scale environment and the distribution of TC genesis (Fig. 12). In our experiments, the maximum SST difference between the warm and cold sectors is limited to 4 K, which is comparable to that in the equatorial Pacific of Earth's present climate. The 4-K SST differences also span across similar spatial scales (~180° longitudinal), leading to comparable zonal gradients of SST in the simulations and Earth's present climate. The impact of the zonally asymmetric SST forcings is relatively minor for the zonal mean precipitable water. But when prescribed between the equator and 20°N, the SST perturbations tend to shift the maxima of precipitation and MPI northward from the equator (Figs. 12c,d). Meanwhile, the vertical wind shear increases equatorward of 15°N across these experiments, even though the shear responses between 15° and 50°N show diverse signs. In comparison, the responses of relative vorticity are more consistent across experiments with positive anomalies near 20°N and negative anomalies near 10° and 40°N. As for TC genesis, zonal asymmetric SST perturbations—except for "W1C1-10N"—tend to decrease the global TC genesis relative to the zonally symmetric reference (b = 0.85) (also see Fig. 11). The majority of this decrease occurs between 5° and 15°N, sometimes amounting to about 50% of the local genesis number in the reference simulation. This decrease is compensated by an increase of genesis near 20°N, shifting the overall genesis latitude poleward. These characteristics of genesis changes are broadly captured by the changes of the GPI, despite some issues in individual experiments (e.g., latitude and sign mismatch in "W1C1-20N").

As expected, the zonal asymmetry of SST forcings also leads to zonally varying circulation responses. Figure 13 shows the regional zonal mean circulation in four experiments ("W1C1-0N," "W1C0-0N," "W1C1-20N," "W1C0-20N"). In the longitudinal sectors with relatively warm SST, the meridional overturning circulation is much more rigorous, and the tropical ascent shifts poleward when the SST perturbations shift from the equator to 20°N. Meanwhile, the zonal wind also shows notable regional variations, especially in the longitudinal

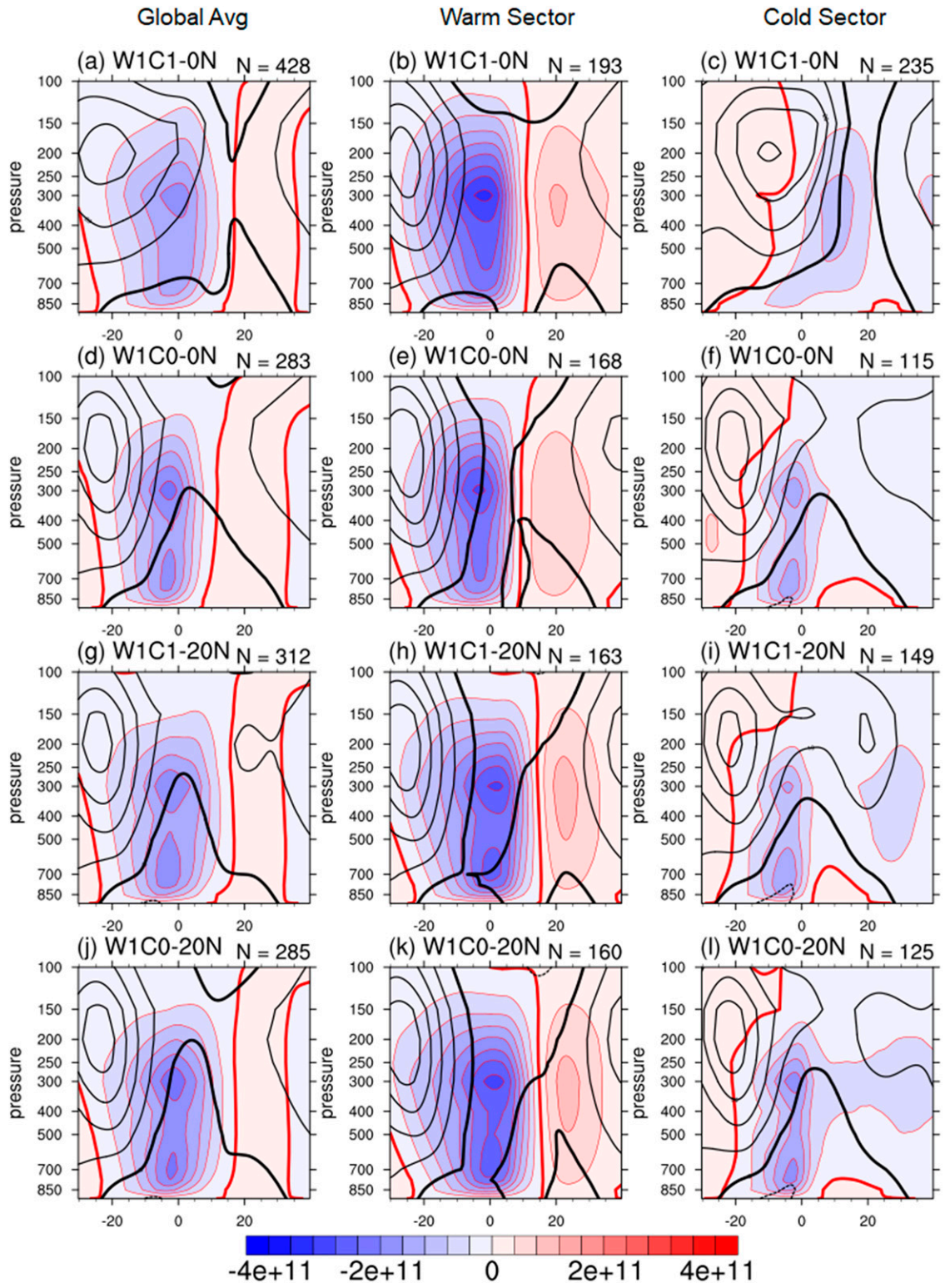

FIG. 13. Zonal averages of the large-scale circulation in the simulations forced by zonally asymmetric SSTs. (a)–(c) W1C1–0N, (d)–(f) W1C0–0N, (g)–(i) W1C1–20N, and (j)–(l) W1C0–20N. (a),(d),(g),(j) The global averages; (b),(e),(h),(k) the averages of the warm sector (270°–0°–90°E); and (c),(f),(i),(l) the averages of the cold sector (90°–180°–270°E). The regional meridional streamfunction has been scaled so that the global and regional results are comparable (Zhang and Wang 2015). The number of TC genesis in individual regions is denoted in the upper-right corners. All the other plotting settings are as in Fig. 7, but the hatching of Ro values is removed.

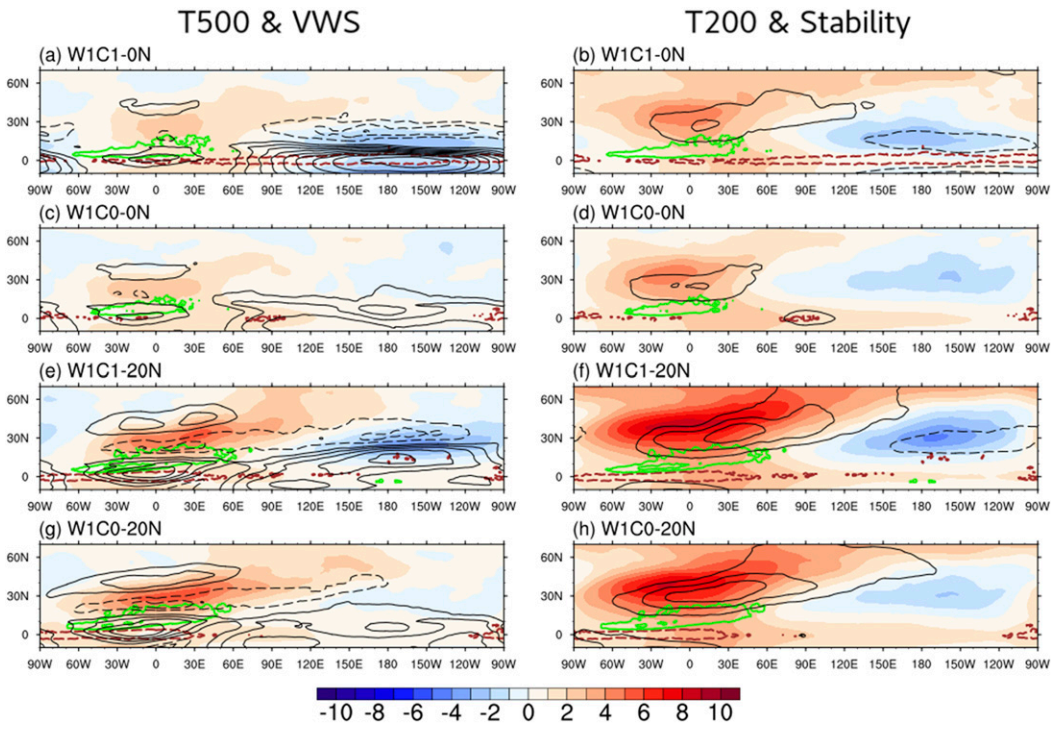

FIG. 14. Environmental responses to zonally asymmetric SST forcings. The responses are the differences between these experiments and the reference experiment with zonally symmetric SST ($b = 0.85$). Green and brown contours show precipitation responses (mm day^{-1}), with contour levels at -5, 5, and 15 mm day^{-1}. (a) Responses of 500-hPa temperature (shading; K) and vertical wind shear (black contours; m s^{-1}) in the W1C1–0N experiment. (b) Responses of 200-hPa temperature (shading; K) and static stability (black contours; K) in the W1C1–0N experiment. The contour interval of the wind shear responses is 5 m s^{-1}. The static stability is defined as the difference between 200-hPa potential temperature and the SST; its contour interval is 2 K. The zero contours of all the variables have been omitted for clarity. The contour levels of (c),(d) W1C0–0N; (e),(f) W1C1–20N; and (g),(h) W1C0–20N are as in (a) and (b).

sectors with relatively cold SST. Regarding the global averages, the "W1C1-0N" and "W1C1-20N" experiments show some notable differences of tropical zonal wind, even though they share the same profile of zonal mean SSTs. This result suggests that regional SST perturbations can strongly affect the zonal mean climate (Figs. 13a,g), including the latitudinal distribution of TCs (Fig. 12g). Interestingly, the four experiments show the equatorial westerly winds (i.e., superrotation), which differ from the reference experiment ($b = 0.85$) and Earth's present-day climate. Detailed discussions of similar circulation changes are available in previous studies (e.g., Mori et al. 2013; Wu and Shaw 2016), and our ensuing discussion will emphasize the relative SST mechanism and TC activity.

c. *Revisiting the relative SST mechanism and TC activity*

We now examine the regionals variations of SST and TC activity (Fig. 11) more closely to evaluate the relative SST mechanism (section 1). Consistent with the relative-SST expectations, warm SST perturbations in the AM4.0-Aqua simulations generally suppress TC genesis in the distant and relatively cold sectors (90°–180°–270°E). For example, when the warm SST perturbations are located at 20°N (Figs. 11e,f), TC genesis number in the cold sector decreases by about 50%–65% relative to the reference simulation (Fig. 11i). However, this relative-SST teleconnection can be complicated by cold-sector SST perturbations in some experiments. One striking case is the "W1C1-0N" experiment, which shows a surprising increase in TC genesis in the cold sector. This increase makes the cold-sector genesis about 20% *more active* than the warm-sector genesis while doubling the cold-sector genesis number relative to the "W1C0-0N" experiment. This large increase of TC genesis in the "W1C1-0N" cold sector contrasts with a decrease that would be anticipated with the relative SST mechanism. Notably, a similar SST–TC relationship is present in the Northwestern Pacific (Sharmila and Walsh 2017), which is located eastward of vigorous off-equator convective activity (i.e., the Asian monsoon system). This similarity suggests that the SST–TC relationship in the "W1C1-0N" experiment is not necessarily an artifact and warrants further investigation.

To investigate why more TCs form over relatively cold SSTs in "W1C1-0N" experiment, we follow the relative SST reasoning and analyze the large-scale environments simulated by the "W1C1-0N" and "W1C0-0N" experiments (Figs. 14a–d). In both experiments, the warm-sector precipitation intensifies near 10°N and helps to warm the overlying free troposphere via the CQE adjustment. Although this warming signal extends

globally, its spatial pattern shows intriguing regional variations that deviate from the homogeneous warming anticipated with the classic WTG picture. In the warm sector, the tropospheric warming is displaced farther poleward relative to the precipitation anomalies, suggesting influences of advective processes and the Rossby wave dynamics (Wu and Shaw 2016). In the cold sector, the tropical troposphere cools instead of warming up with the warm sector. In the "W1C1-0N" experiment, the cooling is centered near 15°N and can reach >2 K. A comparison between "W1C1-0N" and "W1C0-10N" experiments suggests that cold SST anomalies in "W1C1-0N" reduce the near-equator precipitation (Figs. 14a,b), strengthen the cold-sector midtropospheric cooling, and shift the upper-tropospheric cooling equatorward by ~15°. This cooling in "W1C1-0N" is associated with a surprising decrease of the static stability between 10° and 20°N (Fig. 14b), which favors TC activity in a way that would not have been easily anticipated with the relative SST mechanism.

Meanwhile, the meridional temperature gradients in the cold sector of "W1C1-0N" decrease between 15° and 30°N. These subtle gradient changes can be linked to changes of vertical wind shear (~10 m s^{-1}; Fig. 14a) via the thermal wind relationship:

$$\mathrm{VWS} \propto \left(\frac{\nabla \overline{T}}{f}\right), \tag{5}$$

where VWS indicates the vertical wind shear, and $\nabla \overline{T}$ represents the horizontal gradient of the free-troposphere layer-mean temperature, which can be approximated by the 500-hPa temperature. This simple relationship helps to highlight the significance of "weak" temperature gradients—because of the small values of f at low latitudes, even a relatively weak temperature gradient of 2×10^{-3} K km^{-1} (Fig. 1) can be associated with substantial vertical wind shear (>10 m s^{-1}), which can profoundly influence convective activity (e.g., LeMone et al. 1998). In the cold sector of "W1C1-0N" experiment, the tropospheric cooling decreases the meridional temperature gradients between 20° and 30°N, consistent with a decrease of vertical wind shear (Fig. 14a). This shear decrease is also consistent with the unexpected increase of TC genesis (Fig. 11a)–but would have been easily anticipated if the WTG approximation of the tropics is conceptually or mathematically reduced to a zero-gradient state. Overall, the above results suggest that "weak" temperature gradients can have significant influences on convective and TC activity.

For the sake of completeness, the impacts of other large-scale environmental factors are also evaluated. For example, an analysis of 850-hPa relative vorticity in "W1C1-0N" experiment indicates strong positive anomalies in the warm sector and weakly negative anomalies in the cold sector (figure not shown). The warm-sector vorticity increase dominates the zonal-mean vorticity responses (Fig. 12f) but does not directly contribute to the notable increase of TC genesis in the cold sector. Meanwhile, the weak decrease of cold-sector vorticity is inconsistent with the cold-sector TC responses.

A comparison of "W1C1-0N" and "W1C0-0N" experiments with other zonally asymmetric experiments helps to highlight the sensitivity of atmospheric responses to SST forcings. While the patterns of these responses do not seem very sensitive to small changes of the forcing strength [$X = 1, 3$K in Eq. (2)], the regional details are highly sensitive to the latitude (ϕ_1) or the zonal wavenumber (N) of SST perturbations (figures not shown). As an example, here we consider a poleward shift of the wavenumber-1 SST perturbations from the equator to 20°N, namely the "W1C1-20N" and "W1C0-20N" experiments (Figs. 14e–h). These two "20N" experiments show monsoon-like responses that are similar to the aquaplanet experiments by Wu and Shaw (2016). For example, there is strong precipitation between 5° and 25°N in the warm sector, which contributes to pronounced tropospheric warming (maximum > 8 K) that is similar to an upper-tropospheric monsoon ridge. In the tropics, the anomalies of free-troposphere temperature in "20N" and "0N" experiments show only subtle differences, but changes in temperature gradients and vertical wind shear can be substantial in specific regions. For example, consistent with a latitudinal shift of the cold-sector tropospheric cooling, the vertical wind shear near 20°N in the cold sector decreases in "W1C1-0N" (Fig. 14a) but increases in "W1C1-20N" (Fig. 14e); meanwhile, the temperature gradient changes in "W1C0" experiments are weak in the same region, accompanied by weak shear changes (Figs. 14c,g). The sensitivity of wind shear to SST forcings has implications for TC activity in the cold sector (cf. Figs. 11 and 14).

Finally, we note that the discussion here does not fully cover the diverse atmospheric responses in our zonally asymmetric experiments. For example, the cold-sector temperature anomalies are associated with strong off-equator anomalies of the (sub)tropical circulation, which differ from the monsoon-like solution from the Matsuno–Gill linear system. Modeling and observational evidence suggest that these circulation responses—in addition to the CQE-WTG processes—are subject to influences of potential vorticity dynamics (e.g., Wu and Shaw 2016; Ortega et al. 2018) and involve rich tropical–extratropical interactions (e.g., Zhang and Wang 2019; Hoskins et al. 2020; Wang et al. 2020). We emphasize that atmospheric responses to SST perturbations can be model-dependent in aquaplanet simulations (e.g., Nakajima et al. 2013a,b) and leave in-depth discussions to future studies.

5. Summary and discussion

This study conducts aquaplanet experiments using idealized SST forcings to further the physical understanding of the TC–climate relationship. These experiments use a version of the newly developed GFDL AM4 at a relatively high (~50-km grid) resolution (Zhao 2020) and idealized boundary forcings (AM4.0-Aqua). In particular, we use a wide range of SST forcings that sample zonally symmetric and asymmetric variations. The SST forcings differ from previous aquaplanet studies and help us to explore possible responses of TC activity in diverse climate scenarios. The main findings are summarized as follows.

With zonally symmetric specified SSTs that have a maximum at 10°N, reducing the meridional SST gradients around an Earth-like reference state leads to a substantial weakening and southward displacement of the ITCZ, as well as an increase of

the global TC number. Within the experimented parameter space, the increase of TC number is a nearly 100-fold change with many TCs forming at higher latitudes. This large increase of TC genesis is *qualitatively* consistent with the GPI changes. Meanwhile, these high-latitude TCs contribute to negative correlations between the global TC number and the ITCZ latitude/intensity, qualitatively consistent with Fedorov et al. (2019). As high-latitude TCs emerge mostly when the extratropics becomes warmer than Earth's present climate, our findings differ from—but do not necessarily conflict with—earlier observation studies (e.g., Zhang and Wang 2013, 2015) and other aquaplanet simulations that focus on Earth's (perturbed) present climate (Merlis et al. 2013; Ballinger et al. 2015). Reducing the meridional SST gradients also leads to an expansion of the Hadley circulation in the warmer hemisphere. However, the edge of the summer Hadley cell is not well correlated with the latitudes of TC genesis and LMI, mostly due to the experiments with a relatively weak summer Hadley cell. This weak correlation is inconsistent with the conceptual picture proposed by some earlier studies (e.g., Studholme and Gulev 2018; Sharmila and Walsh 2018). Instead, we found that a metric representing the equatorward boundary of baroclinic instability zone is strongly correlated with the latitudes of TC genesis and LMI, especially when the summer Hadley cell is weak or ill defined.

The experiments with zonally asymmetric specified SSTs use a zonally symmetric reference SST profile that resembles Earth's current climate but has amplified high-latitude warming. We found that 2-K SST perturbations with a zonal wavenumber-1 structure alter the tropical circulation structure and tend to reduce the global TC number. Regional SST warming—either with or without prescribed SST cooling at other longitudes within the same zonal band—does not necessarily increase the local TC genesis frequency, even though the warming generally suppresses TC activity in remote regions with relatively cold SSTs. However, this finding has a notable exception for the case of equatorially focused SST anomalies ("W1C1-0N" experiment): a surprising increase of TC genesis can occur over relatively cold SSTs near 20°N, making TC activity in the cold sector overall even more active than that in the warm sector. The regional increase of TC genesis appears to be caused by decreases of vertical wind shear and static stability, which are associated with small but impactful changes of the troposphere temperature. Moreover, the temperature changes in some off-equator tropical regions can be opposite to the expectation based on the CQE-WTG framework and the relative SST mechanism. For example, the mid and upper-troposphere temperature near 15°N can warm at longitudes with positive precipitation anomalies but cool at other longitudes. The findings thus outline a potential limitation of the CQE-WTG framework and may contribute to the ongoing theoretical development for understanding the connections between zonal asymmetric forcings, the tropical circulation, and transient convective activity (e.g., Geen et al. 2020).

A few caveats of our results are worth additional remarks. First, this study focuses on the large-scale dynamics and does not include an in-depth analysis of tropical convective disturbances. These weather- and intraseasonal-scale tropical disturbances move across longitudes and between sectors, and it is possible that their variations modulate regional TC activity. This possibility, as well as other aspects of these tropical disturbances, will be examined in upcoming studies. Furthermore, our atmospheric model experiments omit the radiative seasonal cycle, and our atmospheric model is not coupled to a dynamic ocean. These processes are important for the local and global energy balance, as well as tropical teleconnections (e.g., Chiang and Sobel 2002; Lintner and Chiang 2007). In particular, the absence of ocean coupling complicates the comparison of our results with some earlier studies that include simplified ocean formulations (Merlis et al. 2013; Ballinger et al. 2015). Therefore, inferences from our experiments should not be assumed to apply to the fully coupled climate system without further scrutiny. Finally, we note that responses of atmospheric circulation and convective activity to SST forcings can be highly model-dependent (Nakajima et al. 2013a,b; Stevens and Bony 2013). An intercomparison of models with similar aquaplanet settings may further elucidate interactions between moist processes and the large-scale circulation, as well as help address the underlying uncertainties of our findings.

Overall, the simplified aquaplanet settings allow us to investigate semiempirical relations that are difficult to fully evaluate using observations or complex climate model setups. Although our discussion mostly focuses on the TC–circulation relationship and the relative SST mechanism, this study has other interesting implications. For example, our zonally symmetric experiments cover a wide parameter space and could help to improve or refine empirical genesis indices that were developed based on Earth's present climate. These experiments may also help to interpret paleoclimate records or other idealized simulations, such as the global RCE experiments with coarser resolutions (e.g., Shi and Bretherton 2014; Coppin and Bony 2015) or smaller simulation domains (e.g., Zhou et al. 2014; Wing et al. 2016). Meanwhile, our zonally asymmetric experiments show that even subtle changes in SST forcings can strongly affect environmental variables and TC activity (e.g., average genesis latitude). The sensitivity underscores the challenges in predicting TC activity, as similarly small changes could arise from natural variability and anthropogenic forcings. Finally, our idealized simulations extend the findings by Merlis et al. (2016) and suggest that TC activity beyond the low latitudes can increase substantially with amplified extratropical warming. Its connection with the projected increase of TC-related risks in the subtropics (e.g., Yoshida et al. 2017; Zhang et al. 2020) warrants further investigation.

Acknowledgments. G. Zhang acknowledges the support from National Oceanic and Atmospheric Administration's Predicting and Explaining Extremes Initiative through Princeton University's Cooperative Institute for Modeling the Earth System (CIMES). L. G. Silvers is supported by National Oceanic and Atmospheric Administration Research Grant NA14OAR4320106 and National Science Foundation Grant AGS1830729. We thank Dr. Isaac Held for lectures and conversations that inspired this study. Drs. Hiroyuki Murakami, Nadir Jeevanjee, Yi Ming, Tsung-Lin Hsieh, and Jun Yang provided helpful input for the initial draft. Comments from Dr. Daniel

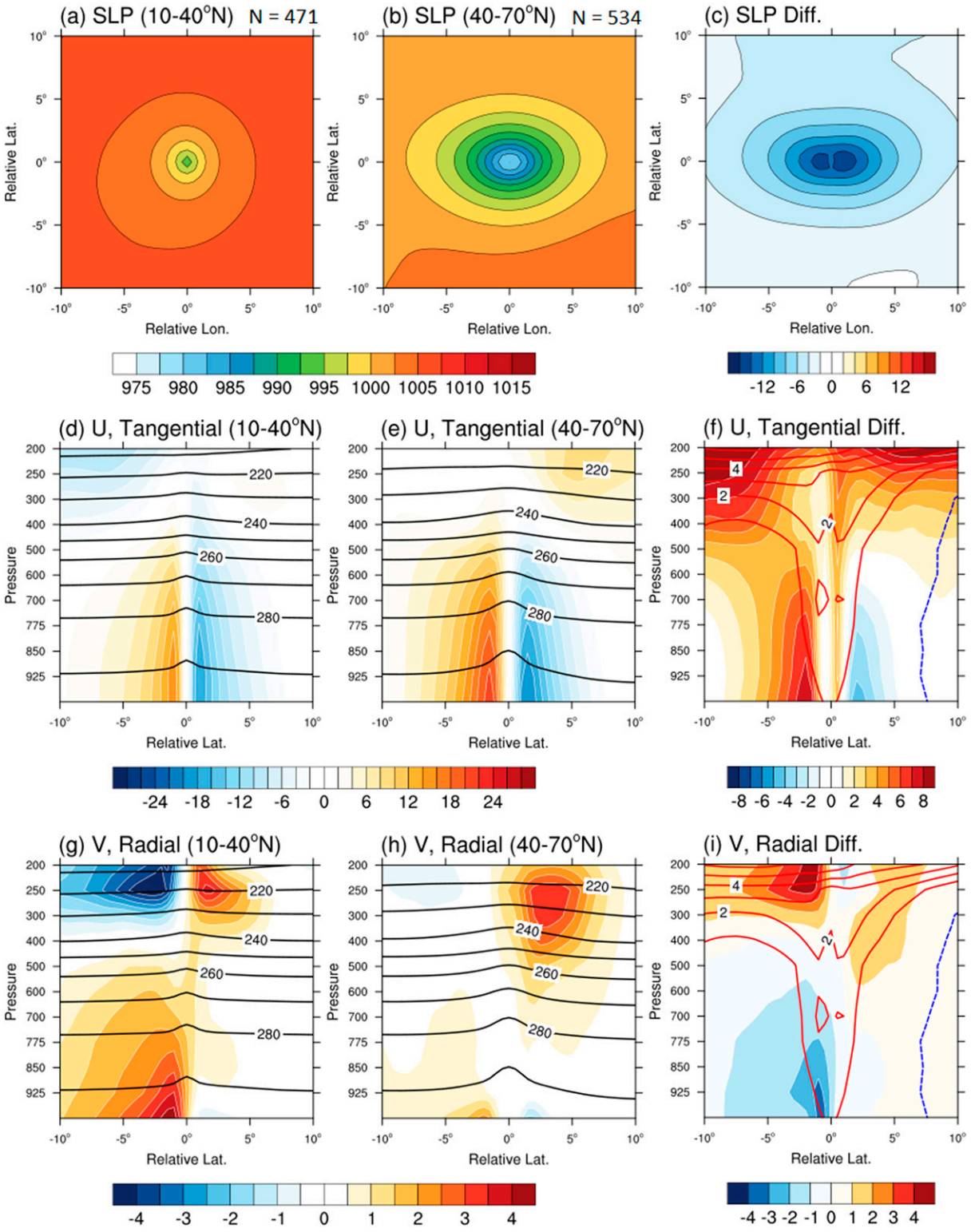

FIG. A1. Storm-centered composites of TCs in the experiment with $b = 0.3$. (a) Sea level pressure (hPa) of storms that reach their lifetime maximum intensity (LMI) between 10° and 40°N. (d) Meridional cross section of tangential wind ($m\,s^{-1}$; zonal wind, color shading) of the same storms. (g) Meridional cross section of radial wind ($m\,s^{-1}$; meridional wind, color shading) of the same storms. The black contours in (d) and (g) show air temperature (K) with contour intervals of 10 K. (b),(e),(h) As in (a), (d), and (g), but for the storms that reach their LMI between 40° and 70°N. (c),(f),(i) Differences of TCs [high-latitude group ($N = 534$) minus low-latitude group ($N = 471$)]. In (f) and (i), the temperature differences are represented with red solid (positive) and blue dashed (negative) contours with 1-K contour intervals.

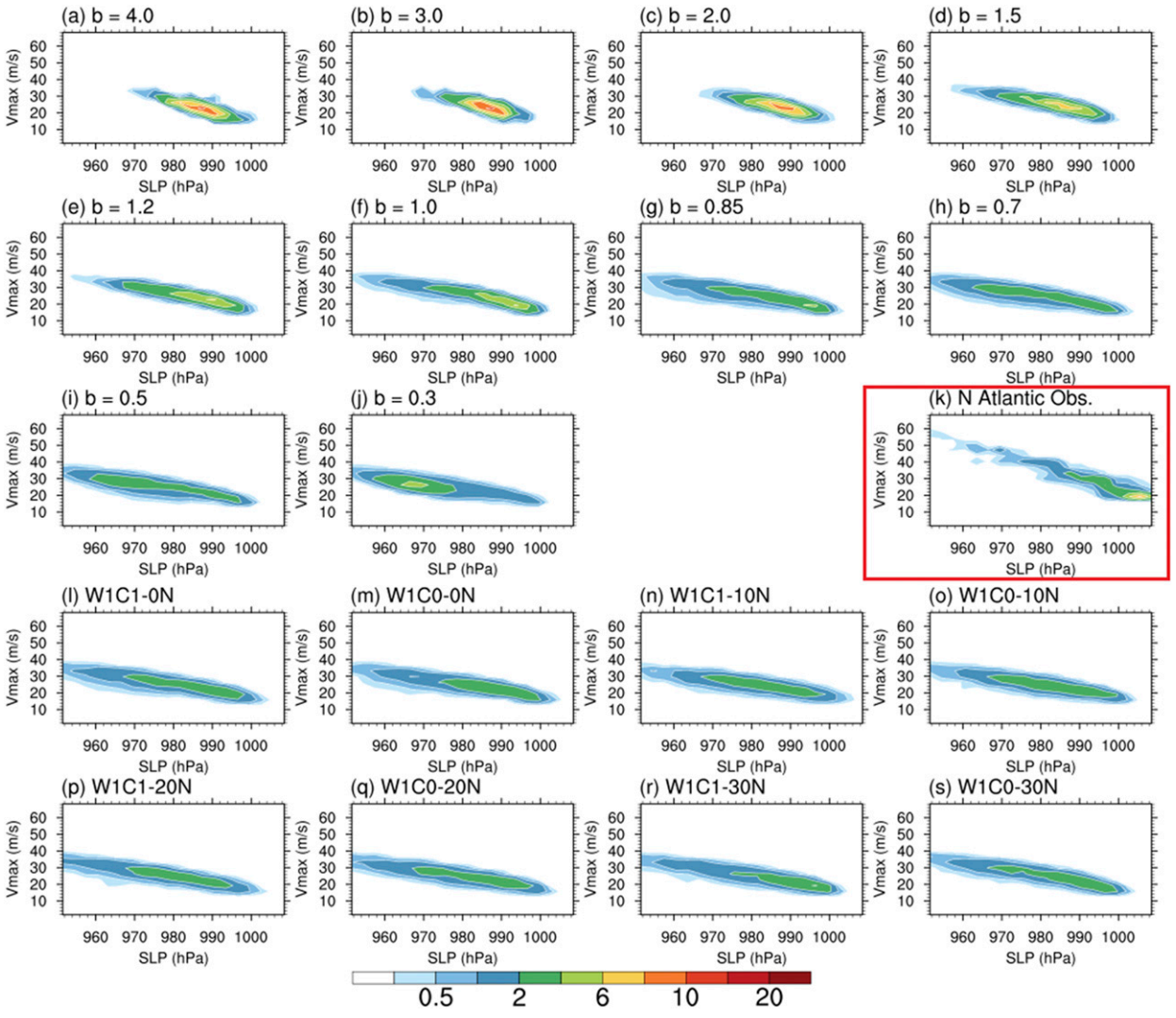

FIG. A2. Relationship of storms' minimum sea level pressure (SLP; hPa) and maximum surface wind ($m\,s^{-1}$) in AM4.0-Aqua experiments and the North Atlantic observation (Knapp et al. 2010). (a)–(j) Experiments with zonally *symmetric* SST forcings (Table 1). (k) The North Atlantic (1979–2013), highlighted with red box. (l)–(s) Experiments with zonally *asymmetric* SST forcings (Table 1). The SST forcings are denoted in the titles of each panel. The color shading shows the two-dimensional probability distribution function of minimum SLP and Vmax. These analyses consider all the data points during the life cycle of individual TCs.

Chavas, Dr. Joshua Studholme, and an anonymous reviewer helped to improve the study in various ways.

Data availability statement. The GFDL AM4 model code is publicly available (http://doi.org/10.5281/zenodo.1199643). The model documentation and code support are available via the GFDL protocol (https://data1.gfdl.noaa.gov/nomads/forms/am4.0/). The data from this study have been archived and are available upon request.

APPENDIX

Model-Simulated Tropical Cyclones

We briefly discuss the structure of TCs simulated by AM4.0-Aqua. Figure A1 shows the composites of storms at their lifetime maximum intensity (LMI) in the experiment with $b = 0.3$. The storms are grouped based on their LMI latitudes (10°–40° and 40°–70°N), and the results are presented in storm-centered relative coordinates (''latitude–longitude'' and ''latitude–pressure''). The two groups of storms show typical TC features: 1) the maximum wind appears at the lower level with a warm-core structure; 2) the primary (tangential-direction) circulation is quasi-circular; 3) the secondary (radial-direction) circulation contributes to low-level convergence and upper-level divergence near the vortex center. The high-latitude group shows a higher intensity and somewhat larger spatial scale, consistent with a similar analysis of an idealized regional simulation with an 18-km resolution (Zhang et al. 2019). The composites also show differences in the upper-level and low-level radial wind, suggesting that the dynamics of

these high-latitude storms and the extensively studied low-latitude TCs may have some differences.

Figure A2 shows the relationship of storms' minimum sea level pressure (SLP) and maximum surface wind speed (Vmax) as two-dimensional probability distribution functions. We present the results from all the AM4.0-Aqua experiments and the observational data of the North Atlantic. All the subplots show a quasi-linear SLP-Vmax relationship despite large differences of storm intensity among the experiments. Compared to the North Atlantic observations, the AM4.0-Aqua plots do not have a pronounced tail of storms with relatively high SLP (>1004 hPa), likely because the tracking algorithm excludes these systems. Meanwhile, the slope of the SLP–Vmax relationship is overly flat as the maximum achievable Vmax in AM4.0-Aqua is clearly too weak compared to observations. A similar bias has been noted by earlier studies (e.g., Zhao et al. 2018a). This SLP–Vmax bias indicates that the structure of simulated storms has some inconsistency with the observation (Davis 2018; Chavas et al. 2017) and warrants future study.

REFERENCES

Annan, J. D., and J. C. Hargreaves, 2013: A new global reconstruction of temperature changes at the last glacial maximum. *Climate Past*, **9**, 367–376, https://doi.org/10.5194/cp-9-367-2013.

Arakawa, A., and W. H. Schubert, 1974: Interaction of a cumulus cloud ensemble with the large-scale environment, Part I. *J. Atmos. Sci.*, **31**, 674–701, https://doi.org/10.1175/1520-0469(1974)031<0674:IOACCE>2.0.CO;2.

Ballinger, A. P., 2015: Tropical cyclone activity in an aquaplanet general circulation model. Ph.D. thesis, Princeton University, 139 pp.

——, T. M. Merlis I. M. Held, and M. Zhao, 2015: The sensitivity of tropical cyclone activity to off-equatorial thermal forcing in aquaplanet simulations. *J. Atmos. Sci.*, **72**, 2286–2302, https://doi.org/10.1175/JAS-D-14-0284.1.

Blackburn, M., and B. J. Hoskins, 2013: Context and aims of the aqua-planet experiment. *J. Meteor. Soc. Japan*, **91A**, 1–15, https://doi.org/10.2151/jmsj.2013-A01.

Bretherton, C. S., and P. K. Smolarkiewicz, 1989: Gravity waves, compensating subsidence and detrainment around cumulus clouds. *J. Atmos. Sci.*, **46**, 740–759, https://doi.org/10.1175/1520-0469(1989)046<0740:GWCSAD>2.0.CO;2.

——, and A. H. Sobel, 2002: A simple model of a convectively coupled Walker circulation using the weak temperature gradient approximation. *J. Climate*, **15**, 2907–2920, https://doi.org/10.1175/1520-0442(2002)015<2907:ASMOAC>2.0.CO;2.

Byrne, M. P., and P. A. O'Gorman, 2013: Land–ocean warming contrast over a wide range of climates: Convective quasi-equilibrium theory and idealized simulations. *J. Climate*, **26**, 4000–4016, https://doi.org/10.1175/JCLI-D-12-00262.1.

Caballero, R., 2007: Role of eddies in the interannual variability of Hadley cell strength. *Geophys. Res. Lett.*, **34**, L22705, https://doi.org/10.1029/2007GL030971.

Camargo, S. J., K. A. Emanuel, and A. H. Sobel, 2007: Use of a genesis potential index to diagnose ENSO effects on tropical cyclone genesis. *J. Climate*, **20**, 4819–4834, https://doi.org/10.1175/JCLI4282.1.

Charney, J. G., 1963: A note on large-scale motions in the tropics. *J. Atmos. Sci.*, **20**, 607–609, https://doi.org/10.1175/1520-0469(1963)020<0607:ANOLSM>2.0.CO;2.

Chavas, D. R., and K. A. Reed, 2019: Dynamical aquaplanet experiments with uniform thermal forcing: System dynamics and implications for tropical cyclone genesis and size. *J. Atmos. Sci.*, **76**, 2257–2274, https://doi.org/10.1175/JAS-D-19-0001.1.

——, ——, and J. A. Knaff, 2017: Physical understanding of the tropical cyclone wind–pressure relationship. *Nat. Commun.*, **8**, 1360, https://doi.org/10.1038/s41467-017-01546-9.

Chen, G., C. Orbe, and D. Waugh, 2017: The role of monsoon-like zonally asymmetric heating in interhemispheric transport. *J. Geophys. Res. Atmos.*, **122**, 3282–3298, https://doi.org/10.1002/2016JD026427.

Chiang, J. C., and A. H. Sobel, 2002: Tropical tropospheric temperature variations caused by ENSO and their influence on the remote tropical climate. *J. Climate*, **15**, 2616–2631, https://doi.org/10.1175/1520-0442(2002)015<2616:TTTVCB>2.0.CO;2.

——, and D. J. Vimont, 2004: Analogous Pacific and Atlantic meridional modes of tropical atmosphere–ocean variability. *J. Climate*, **17**, 4143–4158, https://doi.org/10.1175/JCLI4953.1.

Coppin, D., and S. Bony, 2015: Physical mechanisms controlling the initiation of convective self-aggregation in a general circulation model. *J. Adv. Model. Earth Syst.*, **7**, 2060–2078, https://doi.org/10.1002/2015MS000571.

Daloz, A. S., and S. J. Camargo, 2018: Is the poleward migration of tropical cyclone maximum intensity associated with a poleward migration of tropical cyclone genesis? *Climate Dyn.*, **50**, 705–715, https://doi.org/10.1007/s00382-017-3636-7.

Davis, C. A., 2018: Resolving tropical cyclone intensity in models. *Geophys. Res. Lett.*, **45**, 2082–2087, https://doi.org/10.1002/2017GL076966.

Dee, D. P., and Coauthors, 2011: The ERA-Interim reanalysis: Configuration and performance of the data assimilation system. *Quart. J. Roy. Meteor. Soc.*, **137**, 553–597, https://doi.org/10.1002/qj.828.

Defforge, C., 2016: Evaluating the influence of sea surface temperature on tropical cyclone genesis: Observations and simulations. M.Sc. thesis, Atmospheric and Oceanic Sciences, McGill University, 84 pp.

Emanuel, K. A., 1988: The maximum intensity of hurricanes. *J. Atmos. Sci.*, **45**, 1143–1155, https://doi.org/10.1175/1520-0469(1988)045<1143:TMIOH>2.0.CO;2.

——, 1995: On thermally direct circulations in moist atmospheres. *J. Atmos. Sci.*, **52**, 1529–1534, https://doi.org/10.1175/1520-0469(1995)052<1529:OTDCIM>2.0.CO;2.

——, 2019: Inferences from simple models of slow, convectively coupled processes. *J. Atmos. Sci.*, **76**, 195–208, https://doi.org/10.1175/JAS-D-18-0090.1.

——, J. D. Neelin, and C. S. Bretherton, 1994: On large-scale circulations in convecting atmospheres. *Quart. J. Roy. Meteor. Soc.*, **120**, 1111–1143, https://doi.org/10.1002/qj.49712051902.

Fedorov, A. V., L. Muir, W. R. Boos, and J. Studholme, 2019: Tropical cyclogenesis in warm climates simulated by a cloud-system resolving model. *Climate Dyn.*, **52**, 107–127, https://doi.org/10.1007/s00382-018-4134-2.

Ferreira, R. N., and W. H. Schubert, 1997: Barotropic aspects of ITCZ breakdown. *J. Atmos. Sci.*, **54**, 261–285, https://doi.org/10.1175/1520-0469(1997)054<0261:BAOIB>2.0.CO;2.

Frisius, T., and S. M. A. Abdullah, 2017: Nonlocality of tropical cyclone activity in idealized climate simulations. *J. Adv. Model. Earth Syst.*, **9**, 3099–3115, https://doi.org/10.1002/2017MS001084.

Fueglistaler, S., C. Radley, and I. M. Held, 2015: The distribution of precipitation and the spread in tropical upper tropospheric

temperature trends in CMIP5/AMIP simulations. *Geophys. Res. Lett.*, **42**, 6000–6007, https://doi.org/10.1002/2015GL064966.

Geen, R., S. Bordoni, D. S. Battisti, and K. L. Hui, 2020: Monsoons, ITCZs, and the concept of the global monsoon. *Rev. Geophys.*, **58**, e2020RG000700, https://doi.org/10.1029/2020RG000700.

Gray, W. M., 1984: Atlantic seasonal hurricane frequency. Part I: El Niño and 30 mb quasi-biennial oscillation influences. *Mon. Wea. Rev.*, **112**, 1649–1668, https://doi.org/10.1175/1520-0493(1984)112<1649:ASHFPI>2.0.CO;2.

Hack, J. J., W. H. Schubert, D. E. Stevens, and H.-C. Kuo, 1989: Response of the Hadley circulation to convective forcing in the ITCZ. *J. Atmos. Sci.*, **46**, 2957–2973, https://doi.org/10.1175/1520-0469(1989)046<2957:ROTHCT>2.0.CO;2.

Held, I. M., and B. J. Hoskins, 1985: Large-scale eddies and the general circulation of the troposphere. *Advances in Geophysics*, Vol. 28, Academic Press, 3–31, https://doi.org/10.1016/S0065-2687(08)60218-6.

——, and M. J. Suarez, 1994: A proposal for the intercomparison of the dynamical cores of atmospheric general circulation models. *Bull. Amer. Meteor. Soc.*, **75**, 1825–1830, https://doi.org/10.1175/1520-0477(1994)075<1825:APFTIO>2.0.CO;2.

Herman, M. J., and D. J. Raymond, 2014: WTG cloud modeling with spectral decomposition of heating. *J. Adv. Model. Earth Syst.*, **6**, 1121–1140, https://doi.org/10.1002/2014MS000359.

Hoskins, B. J., G.-Y. Yang, and R. M. Fonseca, 2020: The detailed dynamics of the June–August Hadley cell. *Quart. J. Roy. Meteor. Soc.*, **146**, 557–575, https://doi.org/10.1002/qj.3702.

Hu, Y. Y., L. J. Tao, and J. P. Liu, 2013: Poleward expansion of the Hadley circulation in CMIP5 simulations. *Adv. Atmos. Sci.*, **30**, 790–795, https://doi.org/10.1007/s00376-012-2187-4.

Johnson, N. C., and S.-P. Xie, 2010: Changes in the sea surface temperature threshold for tropical convection. *Nat. Geosci.*, **3**, 842–845, https://doi.org/10.1038/ngeo1008.

Kang, S. M., and J. Lu, 2012: Expansion of the Hadley cell under global warming: Winter versus summer. *J. Climate*, **25**, 8387–8393, https://doi.org/10.1175/JCLI-D-12-00323.1.

Knapp, K. R., M. C. Kruk, D. H. Levinson, H. J. Diamond, and C. J. Neumann, 2010: The International Best Track Archive for Climate Stewardship (IBTrACS). *Bull. Amer. Meteor. Soc.*, **91**, 363–376, https://doi.org/10.1175/2009BAMS2755.1.

Kossin, J. P., K. A. Emanuel, and G. A. Vecchi, 2014: The poleward migration of the location of tropical cyclone maximum intensity. *Nature*, **509**, 349–352, https://doi.org/10.1038/nature13278.

LeMone, M. A., E. J. Zipser, and S. B. Trier, 1998: The role of environmental shear and thermodynamic conditions in determining the structure and evolution of mesoscale convective systems during TOGA COARE. *J. Atmos. Sci.*, **55**, 3493–3518, https://doi.org/10.1175/1520-0469(1998)055<3493:TROESA>2.0.CO;2.

Lintner, B. R., and J. C. H. Chiang, 2007: Adjustment of the remote tropical climate to El Niño conditions. *J. Climate*, **20**, 2544–2557, https://doi.org/10.1175/JCLI4138.1.

Lu, J., G. A. Vecchi, and T. Reichler, 2007: Expansion of the Hadley cell under global warming. *Geophys. Res. Lett.*, **34**, L06805, https://doi.org/10.1029/2006GL028443.

Ma, J., and S.-P. Xie, 2013: Regional patterns of sea surface temperature change: A source of uncertainty in future projections of precipitation and atmospheric circulation. *J. Climate*, **26**, 2482–2501, https://doi.org/10.1175/JCLI-D-12-00283.1.

Mapes, B. E., 1993: Gregarious tropical convection. *J. Atmos. Sci.*, **50**, 2026–2037, https://doi.org/10.1175/1520-0469(1993)050<2026:GTC>2.0.CO;2.

McTaggart-Cowan, R., E. L. Davies, J. G. Fairman Jr., T. J. Galarneau Jr., and D. M. Schultz, 2015: Revisiting the 26.5°C sea surface temperature threshold for tropical cyclone development. *Bull. Amer. Meteor. Soc.*, **96**, 1929–1943, https://doi.org/10.1175/BAMS-D-13-00254.1.

Merlis, T. M., and I. M. Held, 2019: Aquaplanet simulations of tropical cyclones. *Curr. Climate Change Rep.*, **5**, 185–195, https://doi.org/10.1007/s40641-019-00133-y.

——, M. Zhao, and I. M. Held, 2013: The sensitivity of hurricane frequency to ITCZ changes and radiatively forced warming in aquaplanet simulations. *Geophys. Res. Lett.*, **40**, 4109–4114, https://doi.org/10.1002/grl.50680.

——, W. Zhou, I. M. Held, and M. Zhao, 2016: Surface temperature dependence of tropical cyclone-permitting simulations in a spherical model with uniform thermal forcing. *Geophys. Res. Lett.*, **43**, 2859–2865, https://doi.org/10.1002/2016GL067730.

Moon, I.-J., S.-H. Kim, P. Klotzbach, and J. C. L. Chan, 2015: Roles of interbasin frequency changes in the poleward shifts of the maximum intensity location of tropical cyclones. *Environ. Res. Lett.*, **10**, 104004, https://doi.org/10.1088/1748-9326/10/10/104004.

Mori, M., M. Watanabe, and M. Kimoto, 2013: Superrotation and nonlinear Hadley circulation response to zonally asymmetric sea surface temperature in an aquaplanet GCM. *J. Meteor. Soc. Japan*, **91A**, 269–291, https://doi.org/10.2151/jmsj.2013-A10.

Naafs, B. D. A., and Coauthors, 2018: High temperatures in the terrestrial mid-latitudes during the early Palaeogene. *Nat. Geosci.*, **11**, 766–771, https://doi.org/10.1038/s41561-018-0199-0.

Nakajima, K., Y. Yamada, Y. O. Takahashi, M. Ishiwatari, W. Ohfuchi, and Y.-Y. Hayashi, 2013a: The variety of forced atmospheric structure in response to tropical SST anomaly in the aqua-planet experiments. *J. Meteor. Soc. Japan*, **91A**, 143–193, https://doi.org/10.2151/jmsj.2013-A05.

——, ——, ——, ——, ——, and ——, 2013b: The variety of spontaneously generated tropical precipitation patterns found in APE results. *J. Meteor. Soc. Japan*, **91A**, 91–141, https://doi.org/10.2151/jmsj.2013-A04.

Neale, R. B., and B. J. Hoskins, 2000: A standard test for AGCMs including their physical parametrizations: I: The proposal. *Atmos. Sci. Lett.*, **1**, 101–107, https://doi.org/10.1006/asle.2000.0019.

Oort, A. H., and J. J. Yienger, 1996: Observed interannual variability in the Hadley circulation and its connection to ENSO. *J. Climate*, **9**, 2751–2767, https://doi.org/10.1175/1520-0442(1996)009<2751:OIVITH>2.0.CO;2.

Ortega, S., P. J. Webster V. Toma, and H.-R. Chang, 2018: The effect of potential vorticity fluxes on the circulation of the tropical upper troposphere. *Quart. J. Roy. Meteor. Soc.*, **144**, 848–860, https://doi.org/10.1002/qj.3261.

Privé, N. C., and R. A. Plumb, 2007: Monsoon dynamics with interactive forcing. Part I: Axisymmetric studies. *J. Atmos. Sci.*, **64**, 1417–1430, https://doi.org/10.1175/JAS3916.1.

Ramsay, H. A., and A. H. Sobel, 2011: Effects of relative and absolute sea surface temperature on tropical cyclone potential intensity using a single-column model. *J. Climate*, **24**, 183–193, https://doi.org/10.1175/2010JCLI3690.1.

Raymond, D., Ž. Fuchs, S. Gjorgjievska, and S. Sessions, 2015: Balanced dynamics and convection in the tropical troposphere. *J. Adv. Model. Earth Syst.*, **7**, 1093–1116, https://doi.org/10.1002/2015MS000467.

Rayner, N. A., D. E. Parker, E. B. Horton, C. K. Folland, L. V. Alexander, D. P. Rowell, E. C. Kent, and A. Kaplan, 2003:

Global analyses of sea surface temperature, sea ice, and night marine air temperature since the late nineteenth century. *J. Geophys. Res.*, **108**, 4407, https://doi.org/10.1029/2002JD002670.

Rodwell, M. J., and B. J. Hoskins, 2001: Subtropical anticyclones and summer monsoons. *J. Climate*, **14**, 3192–3211, https://doi.org/10.1175/1520-0442(2001)014<3192:SAASM>2.0.CO;2.

Schneider, T., and S. Bordoni, 2008: Eddy-mediated regime transitions in the seasonal cycle of a Hadley circulation and implications for monsoon dynamics. *J. Atmos. Sci.*, **65**, 915–934, https://doi.org/10.1175/2007JAS2415.1.

Schubert, W. H., J. J. Hack, P. L. Silva Dias, and S. R. Fulton, 1980: Geostrophic adjustment in an axisymmetric vortex. *J. Atmos. Sci.*, **37**, 1464–1484, https://doi.org/10.1175/1520-0469(1980)037<1464:GAIAAV>2.0.CO;2.

Seo, J., S. M. Kang, and D. M. W. Frierson, 2014: Sensitivity of intertropical convergence zone movement to the latitudinal position of thermal forcing. *J. Climate*, **27**, 3035–3042, https://doi.org/10.1175/JCLI-D-13-00691.1.

Sharmila, S., and K. J. E. Walsh, 2017: Impact of large-scale dynamical versus thermodynamical climate conditions on contrasting tropical cyclone genesis frequency. *J. Climate*, **30**, 8865–8883, https://doi.org/10.1175/JCLI-D-16-0900.1.

——, and ——, 2018: Recent poleward shift of tropical cyclone formation linked to Hadley cell expansion. *Nat. Climate Change*, **8**, 730–736, https://doi.org/10.1038/s41558-018-0227-5.

Shaw, T. A., and A. Voigt, 2015: Tug of war on summertime circulation between radiative forcing and sea surface warming. *Nat. Geosci.*, **8**, 560–566, https://doi.org/10.1038/ngeo2449.

Shi, X., and C. S. Bretherton, 2014: Large-scale character of an atmosphere in rotating radiative-convective equilibrium. *J. Adv. Model. Earth Syst.*, **6**, 616–629, https://doi.org/10.1002/2014MS000342.

Singh, M. S., Z. Kuang, and Y. Tian, 2017: Eddy influences on the strength of the Hadley circulation: Dynamic and thermodynamic perspectives. *J. Atmos. Sci.*, **74**, 467–486, https://doi.org/10.1175/JAS-D-16-0238.1.

Sobel, A. H., and C. S. Bretherton, 2000: Modeling tropical precipitation in a single column. *J. Climate*, **13**, 4378–4392, https://doi.org/10.1175/1520-0442(2000)013<4378:MTPIAS>2.0.CO;2.

Stevens, B., and S. Bony, 2013: What are climate models missing? *Science*, **340**, 1053–1054, https://doi.org/10.1126/science.1237554.

Studholme, J., and S. Gulev, 2018: Concurrent changes to Hadley circulation and the meridional distribution of tropical cyclones. *J. Climate*, **31**, 4367–4389, https://doi.org/10.1175/JCLI-D-17-0852.1.

Sugi, M., K. Yoshida, and H. Murakami, 2015: More tropical cyclones in a cooler climate? *Geophys. Res. Lett.*, **42**, 6780–6784, https://doi.org/10.1002/2015GL064929.

Tang, B. H., and J. D. Neelin, 2004: ENSO influence on Atlantic hurricanes via tropospheric warming. *Geophys. Res. Lett.*, **31**, L24204, https://doi.org/10.1029/2004GL021072.

Vallis, G. K., 2017: Barotropic and baroclinic instability. *Atmospheric and Oceanic Fluid Dynamics: Fundamentals and Large-Scale Circulation*, 2nd ed. Cambridge University Press, 335–377.

Vecchi, G. A., and B. J. Soden, 2007: Effect of remote sea surface temperature change on tropical cyclone potential intensity. *Nature*, **450**, 1066–1070, https://doi.org/10.1038/nature06423.

——, K. L. Swanson, and B. J. Soden, 2008: Whither hurricane activity? *Science*, **322**, 687–689, https://doi.org/10.1126/science.1164396.

Vimont, D. J., and J. P. Kossin, 2007: The Atlantic meridional mode and hurricane activity. *Geophys. Res. Lett.*, **34**, L07709, https://doi.org/10.1029/2007GL029683.

Walker, C. C., and T. Schneider, 2006: Eddy influences on Hadley circulations: Simulations with an idealized GCM. *J. Atmos. Sci.*, **63**, 3333–3350, https://doi.org/10.1175/JAS3821.1.

Wang, B., B. Xiang, and J.-Y. Lee, 2013: Subtropical high predictability establishes a promising way for monsoon and tropical storm predictions. *Proc. Natl. Acad. Sci. USA*, **110**, 2718–2722, https://doi.org/10.1073/pnas.1214626110.

Wang, C., and G. Magnusdottir, 2005: ITCZ breakdown in three-dimensional flows. *J. Atmos. Sci.*, **62**, 1497–1512, https://doi.org/10.1175/JAS3409.1.

——, and ——, 2006: The ITCZ in the central and eastern Pacific on synoptic time scales. *Mon. Wea. Rev.*, **134**, 1405–1421, https://doi.org/10.1175/MWR3130.1.

Wang, S., and A. H. Sobel, 2011: Response of convection to relative sea surface temperature: Cloud-resolving simulations in two and three dimensions. *J. Geophys. Res.*, **116**, D11119, https://doi.org/10.1029/2010JD015347.

——, ——, and Z. Kuang, 2013: Cloud-resolving simulation of TOGA-COARE using parameterized large-scale dynamics. *J. Geophys. Res. Atmos.*, **118**, 6290–6301, https://doi.org/10.1002/jgrd.50510.

Wang, Z., G. Zhang, T. J. Dunkerton, and F.-F. Jin, 2020: Summertime stationary waves integrate tropical and extratropical impacts on tropical cyclone activity. *Proc. Natl. Acad. Sci. USA*, **117**, 22 720–22 726, https://doi.org/10.1073/pnas.2010547117.

Wing, A. A., S. J. Camargo, and A. H. Sobel, 2016: Role of radiative–convective feedbacks in spontaneous tropical cyclogenesis in idealized numerical simulations. *J. Atmos. Sci.*, **73**, 2633–2642, https://doi.org/10.1175/JAS-D-15-0380.1.

Wu, Y., and T. A. Shaw, 2016: The impact of the Asian summer monsoon circulation on the tropopause. *J. Climate*, **29**, 8689–8701, https://doi.org/10.1175/JCLI-D-16-0204.1.

Yoshida, K., M. Sugi, R. Mizuta, H. Murakami, and M. Ishii, 2017: Future changes in tropical cyclone activity in high-resolution large-ensemble simulations. *Geophys. Res. Lett.*, **44**, 9910–9917, https://doi.org/10.1002/2017GL075058.

Zhang, C., 2005: Madden-Julian Oscillation. *Rev. Geophys.*, **43**, RG2003, https://doi.org/10.1029/2004RG000158.

Zhang, G., and Z. Wang, 2013: Interannual variability of the Atlantic Hadley circulation in boreal summer and its impacts on tropical cyclone activity. *J. Climate*, **26**, 8529–8544, https://doi.org/10.1175/JCLI-D-12-00802.1.

——, and ——, 2015: Interannual variability of tropical cyclone activity and regional Hadley circulation over the Northeastern Pacific. *Geophys. Res. Lett.*, **42**, 2473–2481, https://doi.org/10.1002/2015GL063318.

——, and ——, 2019: North Atlantic Rossby wave breaking during the hurricane season: Association with tropical and extratropical variability. *J. Climate*, **32**, 3777–3801, https://doi.org/10.1175/JCLI-D-18-0299.1.

——, ——, T. J. Dunkerton, M. S. Peng, and G. Magnusdottir, 2016: Extratropical impacts on Atlantic tropical cyclone activity. *J. Atmos. Sci.*, **73**, 1401–1418, https://doi.org/10.1175/JAS-D-15-0154.1.

——, ——, M. S. Peng, and G. Magnusdottir, 2017: Characteristics and impacts of extratropical Rossby wave breaking during the Atlantic hurricane season. *J. Climate*, **30**, 2363–2379, https://doi.org/10.1175/JCLI-D-16-0425.1.

——, T. Knutson, and S. Garner, 2019: Impacts of extratropical weather perturbations on tropical cyclone activity: Idealized sensitivity experiments with a regional atmospheric model. *Geophys. Res. Lett.*, **46**, 14 052–14 062, https://doi.org/10.1029/2019GL085398.

——, H. Murakami, T. Knutson, R. Mizuta, and K. Yoshida, 2020: Tropical cyclone motion in a changing climate. *Sci. Adv.*, **6**, eaaz7610, https://doi.org/10.1126/sciadv.aaz7610.

Zhang, Y., and S. Fueglistaler, 2020: How tropical convection couples high moist static energy over land and ocean. *Geophys. Res. Lett.*, **47**, e2019GL086387, https://doi.org/10.1029/2019GL086387.

Zhao, M., 2020: Simulations of atmospheric rivers, their variability, and response to global warming using GFDL's new high-resolution general circulation model. *J. Climate*, **33**, 10 287–10 303, https://doi.org/10.1175/JCLI-D-20-0241.1.

——, I. M. Held, S.-J. Lin, and G. A. Vecchi, 2009: Simulations of global hurricane climatology, interannual variability, and response to global warming using a 50-km resolution GCM. *J. Climate*, **22**, 6653–6678, https://doi.org/10.1175/2009JCLI3049.1.

——, and Coauthors, 2018a: The GFDL global atmosphere and land model AM4.0/LM4.0: 1. Simulation characteristics with prescribed SSTs. *J. Adv. Model. Earth Syst.*, **10**, 691–734, https://doi.org/10.1002/2017MS001208.

——, and Coauthors, 2018b: The GFDL global atmosphere and land model AM4.0/LM4.0: 2. Model description, sensitivity studies, and tuning strategies. *J. Adv. Model. Earth Syst.*, **10**, 735–769, https://doi.org/10.1002/2017MS001209.

Zhou, W., I. M. Held, and S. T. Garner, 2014: Parameter study of tropical cyclones in rotating radiative–convective equilibrium with column physics and resolution of a 25-km GCM. *J. Atmos. Sci.*, **71**, 1058–1069, https://doi.org/10.1175/JAS-D-13-0190.1.